# 2D KINEMATIC EFFECTS OF 3D DISPLACEMENT FIELDS OF TRIAXIAL SAND COMPRESSION SPECIMENS

A Thesis

by

DEBORA ELIEZER MARTOGI

Submitted to the Office of Graduate and Professional Studies of
Texas A&M University
in partial fulfillment of the requirements for the degree of

MASTER OF SCIENCE

| | |
|---|---|
| Chair of Committee | Zenon Medina- Cetina |
| Committee Members | Sara Abedi |
| | Stephanie German Paal |
| Head of Department | Robin Autenrieth |

August 2017

Major Subject: Civil Engineering

# ABSTRACT

Understanding the development of localization effects, such as shear and compaction bands, observed in sand specimens under compression, has been of research interest to understand elemental soil failure mechanisms. Various experimental and numerical methods had been performed from micro (grain particle level) to macro-scale (soil specimen) level to understand this phenomenon. Recent studies had incorporated different imaging techniques to capture localization effects observed on sand compression specimens. Pictures and its associated displacement fields can be captured during the experiment to study the development of localization effects using digital image correlation technique. The following work aims at a better understanding of the development of localization effects by utilizing continuum mechanics kinematics operators of Three-Dimensional (3D) displacement fields. In addition, continuum kinematics operators are utilized to identify early indications of localization effects.

The proposed methods will include the implementation of divergence, curl, and gradient of displacement fields as defined in MATLAB Calculus Toolbox. The results of the divergence and curl of displacement fields are presented in 2D and while 3D representation is presented for the gradient of displacement field. The use of continuum kinematics operators allows for the identification of compression/ expansion (divergence), rotation (curl), and the rate of compression/ expansion (gradient) in various directions along the surface of the specimens. The effects of varying confining pressure have also been proposed.

The results of kinematics operators' implementation showed that it is possible to identify the development of localization effects as early as the beginning of strain softening or slightly after peak strength. In comparison, the localization effects observed visually by the human eye is found to develop at the end of strain softening towards the beginning of the critical volume. The effect of varying confining pressure affects the clarity, amount, rate, and location of localization observed.

To my family, friends, and those whom I had encountered along the way

ACKNOWLEDGEMENTS

I would like to thank my advisor, Dr. Medina-Cetina for the support and guidance he had provided during this work. I am grateful for the challenges and advices he had provided during this brief study. It has helped me to fulfill one of my long-lasting interests to work on geotechnical research.

I also would like to thank my parents for their continuous support and patience during my study and career away from home. I would not have gone this far without it.

Thank you for my former colleagues and mentors at the ECS Carolinas, LLP who had guided me into the uncertainty of the geotechnical world. Thank you for letting me take this opportunity to fulfill my interest in continuing my studies in soil mechanics. The experience that I had with the company had contributed a lot to my growth as Geotechnical Engineer.

Thank you for all my friends and colleagues in the geotechnical and materials departments who had always made my graduate study fun and enjoyable. Thank you also to my friends who pulled me away to take a break and refresh. All of you had made my experience at Texas A&M University incredible.

## CONTRIBUTORS AND SOURCE OF FUNDING

The following work was supervised by thesis chair committee, Dr. Medina-Cetina. The data analyzed prior to performing this analysis (Chapter 2) were conducted by Dr. Medina-Cetina as part of his Ph.D. dissertation titled "Probabilistic Calibration of a Soil Model" published in 2006.

Additional data (Chapter 2) has also been provided by Ahran Song as part of her Ph.D. dissertation titled "Deformation Analysis of Sand Specimens using 3D- Digital Image Correlation for the Calibration of an Elasto- Plastic Model" which were completed in 2012.

All other work conducted for this thesis was completed independently under the advisement of Dr. Medina-Cetina.

In addition, the following work is based on the algorithm developed in CVEN 651-Geomechanics course. Additional algorithm was developed independently through MATLAB algorithm.

No funding is associated with the following work.

TABLE OF CONTENTS

Page

ABSTRACT ..... ii

DEDICATION ..... iv

ACKNOWLEDGEMENTS ..... v

CONTRIBUTORS AND FUNDING SOURCES ..... vi

TABLE OF CONTENTS ..... vii

LIST OF FIGURES ..... ix

LIST OF TABLES ..... xiii

1 INTRODUCTION AND LITERATURE REVIEW ..... 1

2 SOIL EXPERIMENT AND 3D- DIC ..... 7

2.1 Soil Experiment ..... 7
2.2 Digital Image Correlation (DIC) ..... 9
2.3 3D- DIC DATA CORRECTION ..... 13
2.4 Cumulative Displacement ..... 15

3 KINEMATIC ANALYSIS ..... 18

3.1 Geomechanical Framework ..... 18
3.1.1 Descriptions ..... 20
3.1.2 Data Implementation ..... 23
3.1.3 Displacement Fields ..... 24
3.2 Kinematic Operators ..... 30
3.2.1 Divergence and Curl ..... 30
3.2.2 Gradient ..... 32

4 MATLAB IMPLEMENTATION ..... 36

4.1 Summary of Missing Points ..... 36
4.2 Displacement Fields ..... 37
4.2.1 Cartesian Displacement Fields ..... 37

4.2.2 Cylindrical Displacement Fields ..... 46
4.3 Divergence of Displacement Fields ..... 55
4.4 Curl of Displacement Fields ..... 59
4.5 Deformation Gradient ..... 63

5 SUMMARY AND CONCLUSIONS ..... 68

REFERENCES ..... 71

LIST OF FIGURES


Page

Figure 2.1 Reduced stress- strain curves (Medina, 2006; Song, 2012) ..... 9

Figure 2.2 (a) Geocomp Triaxial setup (b) Geocomp Triaxial and 3D- DIC Setup (c) Absolute error of displacement measurement (Reprinted from Medina, 2006) ..... 12

Figure 2.3 Histogram of selected case of rotation angle analysis (Reprinted from Medina and Song, 2012) ..... 13

Figure 2.4 Correction to tilting observed (Reprinted from Medina and Song, 2012)..... 14

Figure 2.5 Alignment of coordinate system (Reprinted from Medina and Song, 2012)..... 15

Figure 2.6 Interpolation and extrapolation between image no. 000 with no. 008, 0.4% axial strain step (Reprinted from Medina and Song, 2012) ..... 16

Figure 3.1 Test 121304a (40kPa): Test 121304a (40 kPa): (Left) Undeformed/ material configuration at 0% strain; (Right) Deformed/ spatial configuration at 7.2 % strain ..... 19

Figure 3.2 Tests 121304c (60 kPa): Divergence at 10% axial strain in Lagrangian (left) and Eulerian (right) descriptions ..... 22

Figure 3.3 Test 121304d (20kPa) Lagrangian Displacement at 3.6%, 5.2%, and 7.2% axial strain. (Left) Material displacement in x- direction. (Middle) Material Displacement in y-direction. (Right) Material Displacement in z- direction..... 26

Figure 3.4 Test 121304d (20kPa) Eulerian Displacement at 3.6%, 5.2%, and 7.2% axial strain. (Left) Material displacement in x- direction. (Middle) Material Displacement in y-direction. (Right) Material Displacement in z- direction..... 27

Figure 3.5 (Left) Cylindrical coordinate system in MATLAB (MATLAB, 2017) (Right) Cartesian coordinate system used in analysis (Reprinted from Song, 2012)..... 29

Figure 3.6 Test 121304a Material divergence subsets at 7.8%, 8.8%, 9.4%, and 10.2%..... 31

Figure 3.7 Test 121304a Material curl subsets at 8.2 to 8.6%, 8.6 to 9%, 9 to 9.4%, and 9.4 to 9.8% axial strain..... 32

Figure 3.8 Test 121304c: Subset of points 15001 , 15002, and 15323 at undeformed configuration (0% axial strain) and 11.2% axial strain... 33

Figure 4.1 Percentage of missing spatial points for all tests in spatial description with 0.8 % axial strain step ..... 37

Figure 4.2 Test 121304d (20 kPa)- Picture of digital images (Medina, 2006) and plot of Displacement (cartesian) in Lagrangian Description at 3. 2%, 5.6%, 7.2%, and 10% axial strain. (Left) x- direction, (Middle) y-direction, (Right) z-direction. ..... 39

Figure 4.3 Test 121304d (20 kPa)- Picture of digital images and plot of Displacement (cartesian) in Eulerian Description at 3. 2%, 5.6%, 7.2%, and 10% axial strain. (Left) x- direction, (Middle) y- direction, (Right) z-direction. ..... 40

Figure 4.4 Test 121304a (40 kPa)- Picture of digital images (Medina, 2006) and plot of Displacement (cartesian) in Lagrangian Description at 3. 2%, 5.2%, 7.2%, and 10% axial strain. (Left) x- direction, (Middle) y-direction, (Right) z-direction. ..... 41

Figure 4.5 Test 121304a (40 kPa)- Picture of digital images (Medina, 2006) and plot of Displacement (cartesian) in Eulerian Description at 3. 2%, 5.2%, 7.2%, and 10% axial strain. (Left) x- direction, (Middle) y-direction, (Right) z-direction. ..... 42

Figure 4.6 Test 121304c- Digital Images (Medina, 2006) and Displacement (cartesian) in Lagrangian Description at 3. 2%, 5.2%, 7.2% and 10% axial strain. (Left) x- direction, (Middle) y- direction, (Right) z-direction. ..... 43

Figure 4.7 Test 121304c- Digital Images (Medina, 2006) and Displacement (cartesian) in Eulerian Description at 3. 2%, 5.2%, 7.2% and 10% axial strain. (Left) x- direction, (Middle) y- direction, (Right) z-direction..... 44

Figure 4.8 Off- centered bulging observed. Figure shown is at 10% axial strain level. From left to right: 121304b (loose), 121304c (60 kPa), 121304d (20kPa) ..... 45

Figure 4.9 121304d (20kPa) Cylindrical Displacement in Lagrangian Description at 3.2%, 5.2%, 7.6%, and 10% axial strain. From left to right: radial displacement, tangential/ angular displacement, and vertical displacement ..... 47

Figure 4.10 121304d (20kPa) Cylindrical Displacement in Eulerian Description at 3.2%, 5.2%, 7.6%, and 10% axial strain. From left to right: radial displacement, tangential/ angular displacement, and vertical displacement ..... 48

Figure 4.11 Test 121304a (40 kPa)- Displacement (cylindrical) in Lagrangian Description at 3. 2%, 5.2%, 7.2%, and 10% axial strain. (Left) radial, (Middle) tangential, and (Right) y-direction. ..... 49

Figure 4.12 Test 121304a (40 kPa)- Displacement (cylindrical) in Eulerian Description at 3. 2%, 5.2%, 7.2%, and 10% axial strain. (Left) radial, (Middle) tangential, and (Right) y-direction. ..... 50

Figure 4.13 121304c (60 kPa) Cylindrical Displacement in Lagrangian Description at 3.2%, 5.2%, 7.6%, and 10% axial strain. From left to right: radial displacement, tangential/ angular displacement, and vertical displacement ..... 51

Figure 4.14 121304c (60 kPa) Cylindrical Displacement in Eulerian Description at 3.2%, 5.2%, 7.6%, and 10% axial strain. From left to right: radial displacement, tangential/ angular displacement, and vertical displacement ..... 52

Figure 4.15 Vertical pattern in angular displacement. From left to right: 121304a tangential displacement at strain levels 0.4% and 0.8%, 101304a tangential displacement at 0.2% and 0.6% strain levels ..... 54

Figure 4.16 Test 121304b (Loose) - Formation of shear band due to contrasting tangential displacement initiated at lower left of specimen. Axial strain levels from left to right: 1.6%, 2.8%, 3.2%, 4.4%, and 5.2% ... 54

Figure 4.17 121304d (20 kPa) Divergence in Lagrangian Descriptions (Top) and Eulerian Description (Bottom) at 1.6%, 3.2%, 5.2%, 7.6%, and 10% axial strain ..... 56

Figure 4.18 121304a (40 kPa) Divergence of displacement field at 1.6%, 3.2%, 5.2%, 7.2%, and 10% axial strain. (Top) Lagrangian Description. (Bottom) Eulerian Description..... 57

Figure 4.19 121304c (60 kPa) Divergence at 1.6%, 3.2%, 5.2%, 7.2%, and 10% in Lagrangian Description (Top) and Eulerian Description (Bottom).. 58

Figure 4.20 121304d (20 kPa) Curl in Lagrangian Description (TOP) and Eulerian Description (Bottom) at 1.6%, 3.2%, 6%, 7.2%, and 10% axial strain..... 60

Figure 4.21 121304a- Curl in Material Description (Top) and Eulerian Description (bottom) at 1.6%, 3.2%, 6%, 7.6%, and 10% axial strain. 61

Figure 4.22 121304c (60 kPa) Curl in Lagrangian Description (Top) and Eulerian Description (Bottom) at 1.6%, 3.2%, 6%, 7.2%, and 10% axial strain 62

Figure 4.23 121304a (40 kPa)-Deformation gradient at 0.8% and 3.2% axial strain. From left to right: x, y, and z- direction deformation gradient.. 64

Figure 4.24 121304d (20 kPa)-Deformation gradient at 3.2%, 5.2%, 7.6 % and 10% axial strain. From left to right: x, y, and z- direction deformation gradient ..... 66

Figure 4.25 121304c (60 kPa)-Deformation gradient at 3.2%, 5.2%, 7.6 % and 10% axial strain. From left to right: x, y, and z- direction deformation gradient. ..... 67

LIST OF TABLES

Page

Table 2.1 Experimental Data (Reprinted from Medina, 2006; Song, 2012) ..... 8

Table 2.2 Reduced summary of rotation angle analysis (Reprinted from Medina and Song, 2012) ..... 13

Table 3.1 Cartesian to cylindrical coordinate system conversion..... 29

# 1. INTRODUCTION AND LITERATURE REVIEW

The failure mechanism in geomaterials had been associated with the presence of localization effects, such as shear and compaction bands (Besuelle and Rudnicki, 2003). Various experimental and numerical techniques had been performed to understand deformation in granular material at the micro- scale level (grain particle level), meso- scale level (grain cluster), and the macro- scale levels (Abedi, 2012; Alshibli, 2001; Iwashita & Oda, 2000; Medina-Cetina, 2006; Rechenmacher & Saab, 2002). Traditionally, experimental technique had been carried out using triaxial and biaxial test at the macro-scale level. Correlations were then performed on the formation of localization effects with the constitutive theory of granular materials (Desrues, 2004; Mooney et al, 1998). The constitutive models developed at the macro- scale levels typically yield to global, averaged material response (Viggiani and Hall, 2008).

Recent development in imaging techniques had made possible the characterization and quantification of localization effects at a finer scale. Based on the aim of measurements, two types experimental imaging techniques can be defined (Rechenmacher and Finno, 2004). The first category measures the density variations between the shear bands and surrounding materials (Alshibli, 2001; Desrues, 2004; Hall et al, 2010; Higo et al, 2013;), while full- field displacement is measured in the second category (Iwashita and Oda, 2000; Medina-Cetina, 2006; Rechenmacher, 2005; Song, 2012).

In first approach, X-ray Computed Tomography (XRCT or X-ray Micro-CT) and Synchrotron Micro- Tomography (SMT) had been utilized in studying the density variation observed within shear bands and surrounding materials. The internal characteristic of the development of localization effects had also been studied by Alshibli et al (2000). More recent studies had incorporate kinematics effects at the micro- scale level. Hall et al (2010) utilized CT scan and developed ID- Track, a discrete particle tracking method, to determine particle translational and rotational fields (particle kinematics). Cil et al. (2014) investigated the 3D kinematics and strength behavior of granular materials in micro- scale level. 3D X-ray Diffraction (3D- XRD) was utilized to measure volume averaged lattice strain of individual grains under 1D compression loading. This was performed to understand the force transmission mechanism of granular sand particles within the granular structure. Overall, CT method is an effective method to capture density variations and micro-scale kinematics. However, testing with CT technique cannot be performed under typical confinement applied on traditional tests due to the required radiation source (Rechenmacher et al, 2013).

The full- field measurement had been utilized in the study of development of localization effects since 1963 (Viggiani and Hall, 2008). X- Ray radiography (Roscoe et al, 1963) and False Relief Stereophotogrammetry (Butterfield, 1970; Desrues and Viggianni, 2004) were used to measure strain field and full- field displacement of soil deformation. Recently, the Digital Image Correlation (DIC) technique had been used extensively to measure triaxial specimens incremental surface displacement based on the boundary information obtained on a sequence of images captured during triaxial testing at

a specified strain rate (Sutton et al, 2009). The results from DIC Analysis performed in previous studies had yield to information on shear band evolution as function of stress-strain, deformation, kinematics (Abedi, 2012; Omidvar et al 2015), spatial density (Rechenmacher et al, 2012), void ratio, force chains (Rechenmacher et al, 2011), and volume correlation utilizing Digital Volume Correlation (Sjödahl Et al, 2012).

In addition, formation of columnar structure referred as force chains had also been observed by Rechenmacher et al (2006, 2011). The study utilized VIC- 2D and VIC- 3D to process DIC data obtained on true triaxial test on the sand specimen. Randomly spaced force chains were observed to periodically developed and collapse at the critical state. Initiation of shear, rotational, and volumetric strain is an indication of force chain buildup and collapse. The periodic spacing of force chains is observed during the softening period. Force chain mechanism had also been observed by Iwashita and Oda (2000) and Higo et al (2013).

Limited studies had been observed on correlating the results of various image correlation methods with continuum kinematic operators such as divergence, curl, and gradient in studies of soil deformation. Coupled imaging correlation technique and kinematics studies had been applied in various field including but not limited to biomedical engineering, structural mechanics, geodynamics, geosciences, and material sciences. In the field of biomedical engineering, kinematics operators such as divergence and curl were utilized to improve anatomical landmark error of warped images (Riyahi-Alam et al, 2014). Studies of deformation field and gradient of deformation to derive strain with DIC technique had been utilized in characterization of localization phenomena in

steels during necking (Wattrisse et al, 2001), artic ice kinematics (Tschudi et al, 2008), and study on Valoria Landslide using LIDAR survey data (Daehne and Corsini, 2013).

In the field of soil mechanics, numerous studies had been performed to validate large soil deformation using Finite Element Method (FEM), Finite Difference Method (FDM), or DEM. FEM and FDM are typically used to model material at the macroscopic level while DEM is used to model at the microscopic (particle) level. FDM are used in solving numerical time-dependent analysis of stresses and strain while similar analysis is performed through spatial discretization in FEM. FEM was the first numerical approach which allows the assignment of different properties into different finite elements. Therefore, heterogeneity can be considered in FEM analysis. However, FEM capability is restricted in solving continuum problem involving discontinuities due to failure, cracking and damaged (Ibrahimbegovic, 2009; Wriggers, 2008; Nikolic, 2016). In addition, soil large deformation at higher strain may exceed the finite elements size, therefore, leading to severe mesh distortions if not enough care is taken in setting up the system rigidity matrix (Boldyrev and Muyzemnek, 2008).

ABAQUS, a FEM program, had been used to simulate localization effects observed during triaxial Consolidated Drained test (CD) on dry sieved construction sand specimen (Song, 2012). 3D- DIC technique was used to obtain the deformation of a representative volume of the sand which is later used to characterize the kinematics and volumetric behavior at various strain levels. Details of this study will be discussed later as it is related to the following work. In addition, the localization effects observed at the meso- scale

level on biaxial test of sand specimen had also been validated using FEM in study performed by Abedi (2012).

DEM approach was developed to consider FEM limitations with model discontinuities. DEM is capable of modeling assembly of particles interactions and simulates their finite displacements and rotations. PFC3D, a DEM program, has been utilized to validate triaxial test experiment performed with CT imaging technique (Cil and Alshibli, 2014). White plastic "pearls" were used in the experiment to allow tracking of solid spherical particles. The result of the PFC3D simulation over predicted the translation and rotational kinematics when compared with the experimental results of the triaxial experiment using and CT which characterized particles 3D kinematics by tracking the evolution of translation and rotation of particles. The simulation in PFC3D was performed with two boundary conditions, flexible membrane boundary and fixed membrane boundary. Both approaches yield similar results in particle rotation distribution but better prediction and characteristic of deformation is obtained with the flexible boundary model.

The work on soil kinematics based on DIC techniques has also been performed with MATLAB algorithm. MATLAB was utilized to obtain the displacement field and shear strains in the study of soil deformation around uplift anchors in air- dried- sand (Liu et al, 2012) and in the study of mesoscale and macroscale behavior of granular soils during plane strain pile penetration (Omidvar et al, 2014). In addition, the volumetric strain was also determined as the summation of the normal strain components by Liu et al (2012). The work by Omidvar also includes estimation of deformation gradient using constant strain triangle with linear strain triangles. In a study on meso- scale kinematics of shear

band development in sand performed by Abedi (2012), decomposition of deformation gradient into symmetrical stretch tensor and orthogonal tensor was performed to obtain the rotational angle.

Not much study has considered the application of divergence and curl operators into soil kinematics study. The following study is performed to observe and characterize the localization effects of sand specimens under compression using continuum mechanics kinematics operators of Three-Dimensional (3D) displacement fields. In doing so, MATLAB Calculus toolbox will be utilized to implement the continuum kinematic operators (divergence, curl, and gradient) of 3D displacement fields obtained from the DIC technique. An analysis will also be performed on the effects of varying confining pressure on the development of localization effects.

# 2. SOIL EXPERIMENT AND 3D-DIC*

## 2.1 Soil Experiment

The following study is performed based on data collected on triaxial consolidated drained (CD) tests performed utilizing 3D-DIC (Medina, 2006; Song, 2012). The tests were performed based on modified ASTM D 4767, standard Consolidation Drained (CD) compression test. An automated triaxial device by Geocomp was used in the experiment. The plexiglass was removed to avoid reflection and refraction effects from cell fluid and light. This modification would allow more controlled and better testing environment for the 3D- DIC technique. Due to the removal of plexiglass, the experiment is performed on dry sand tested under confinement pressure applied using a vacuum pump. Two vaccum pumps were utilized to apply constant confining pressure, which allow volume change with the increase in deviatoric stress. The resulting deviatoric/ effective stress is similar to that of the conventional CD test where the soil is saturated.

The experiment is performed on dry sieved construction sand, classified as SP, with specific gravity ($G_s$) of 2.63 and mean diameter ($D_{50}$) of 0.5 mm. The coefficient of curvature and uniformity of the sand were determined to be $C_u$= 2.34 and $C_c$= 1.11. Sieved construction sand was selected for the experiment to provide adequate color spectrum during imaging analysis. Specimens were compacted in three layers through vibratory compaction method (mold tempered) and dry pluviation method. The relative density ($D_r$) of the samples ranges from 85% to 95%. In addition, one loose specimen with $D_r$ of 46.39% and a layered specimen with $D_r$ of 68.9% were also tested. Most tests were

*The following chapter is based on previous work by Medina-Cetina (2006) and Song (2012)

performed at 40 kPa confining pressure with exceptions to three tests consolidated at 20 kPa and 60 kPa. The tests were performed at a controlled deformation rate of 0.2 % of axial strain/ min. Selected experimental data to be analyzed in this study is presented in Table 2.1.

The global stress- strain curves for all tests are presented in Figure 2.1. No peak stress is observed for the loose specimen. The residual strength of the loose specimen is 150 kPa. The specimen tested at 20 kPa confining pressure has peak strength of 140 kPa and residual strength of 98 kPa. The peak deviatoric stress of compacted sand specimens tested under 40 kPa confinement pressure ranges from 220 to 255 kPa. The corresponding residual deviatoric stress observed ranges from 155 to 185 kPa. The peak deviatoric stress of the dense specimen tested under 60 kPa confinement pressure (121304c) is 359 kPa with the associated residual deviatoric stress of 265 kPa. The increase in the difference between the peak shear strength and the residual strength is observed with the increase in confining pressure.

**Table 2. 1 Experimental Data (Reprinted from Medina, 2006; Song, 2012)**

| TEST ID | D (mm) | H (mm) | $\rho$ (kg/m$^3$) | Dr (%) | Notes |
|---|---|---|---|---|---|
| 121304d | 71.38 | 159.50 | 1736.71 | 99.71 | Dry Pluviation, 20 kPa |
| 121304a | 71.30 | 160.00 | 1721.84 | 94.73 | Dry Pluviation, 40 kPa |
| 101204a | 71.46 | 160.00 | 1708.00 | 90.09 | Dry Pluviation, 40 kPa |
| 121304b | 70.86 | 158.17 | 1588.84 | 46.39 | Dry Pluviation, 40 kPa Loose |
| 121304c | 70.48 | 160.00 | 1718.72 | 93.72 | Dry Pluviation, 60 kPa |

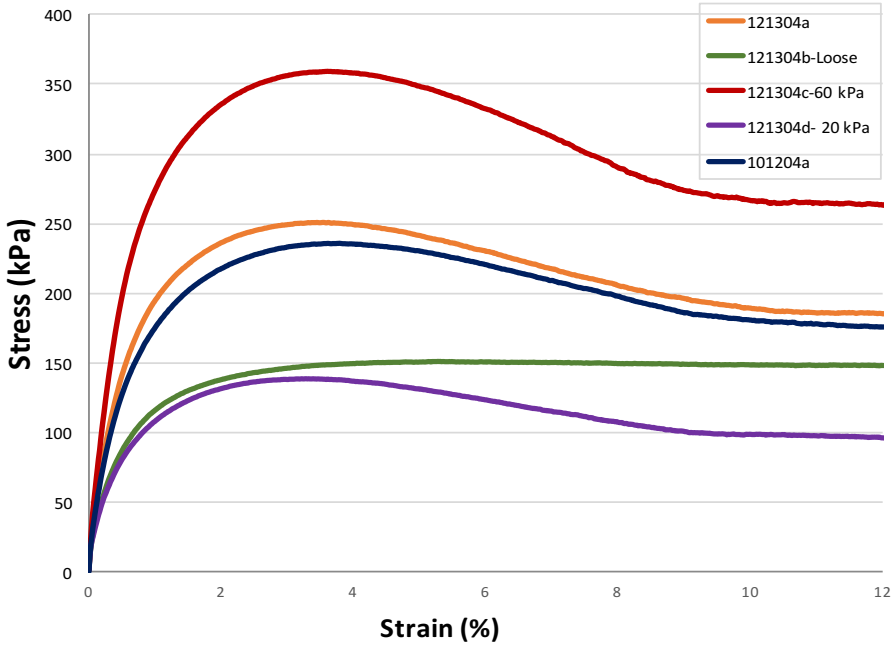


**Figure 2. 1 Reduced stress- strain curves (Reprinted from Medina, 2006; Song, 2012)**

## 2.2 Digital Image Correlation (DIC)

Digital Image Correlation (DIC) method had been utilized to capture the deformation and localization phenomena in this experiment. An outline of the development of two- dimensional (2D) and three- dimensional (3D) DIC can be found in Sutton et al. (2000). Studies of localization effects in sand triaxial/ biaxial tests had been performed utilizing 2D- DIC (Rechenmacher and Finno, 2004) and 3D- DIC (Rechenmacher and Medina-Cetina, 2006; Medina-Cetina and Song, 2012). The 2D- DIC technique yields to deformation information of 2D planar surface while 3D surface and volumetric information can be obtained using the 3D- DIC technique.

The experiment utilizes the 3D-DIC technique in which two cameras capture sequence of images taken every 15 seconds or 0.05% axial strain. The cameras being used during the experiment are 14- bit digital Q-IMAGING PMI-4201 with 4.2MP resolution (2024x 2024 pixels), which are set 25 cm apart and mounted on tripods located 50 cm away from the sample (figure 2.2a and 2.2b). The surface or boundary information is obtained by VIC-3D software developed by Correlated Solutions (2004). VIC- 3D translated the pictures taken at various strain levels into 3D full- field displacement. The pictures were taken on 1/3 of the sample parameter of which region of interest is selected from the first frame.

Within the area of interest (common section of two cameras), seed window is defined for images captured by the two cameras. The seed window identified the common pixels between two frames. This process is also known as pattern recognition. To avoid unrecognizable pattern due to out of frame pattern, the reference image is updated every fourth picture or every 0.2% axial strain. Therefore, the resulting displacement field processed by VIC-3D is an incremental displacement field.

Subsets were set to 45 pixels by 3 pixels. This yields to approximate displacement vectors spacing of 0.4 mm (Medina, 2006) across the sample surface area of interest. This resolution should be sufficient to capture the grain- scale resolution of displacements for the sand specimen with a mean diameter of 0.5 mm, classified as poorly graded sands (SP). Non- integer pixel displacements shown in gray levels are interpolated using cubic interpolation to ensure continuous intensity distributions.

The reference frame identified from VIC- 3D calibration is defined in the 3D Cartesian system (x,y,z). The associated 3D displacement fields for each strain levels are recorded for calibration up to 12% strain, at which local deformation is difficult to be traced beyond this strain level (Song, 2012). The 3D- displacement fields describing the deformed configuration are defined as u,v,w for each corresponding x,y, and z directions. The results of vertical displacement obtained through DIC were compared to measured vertical displacement recorded using LVDT transducer during the experiment. Summary of the comparison statistics can be found in figure 2.2c (Medina, 2006). Based on the comparison, the mean absolute error was determined to be 0.00 mm, with a standard deviation of 0.02 mm. Similar accuracy should be observed in the horizontal in- plane (u) and out- of- plane (w) displacements based on previous observation by Sutton (2000).

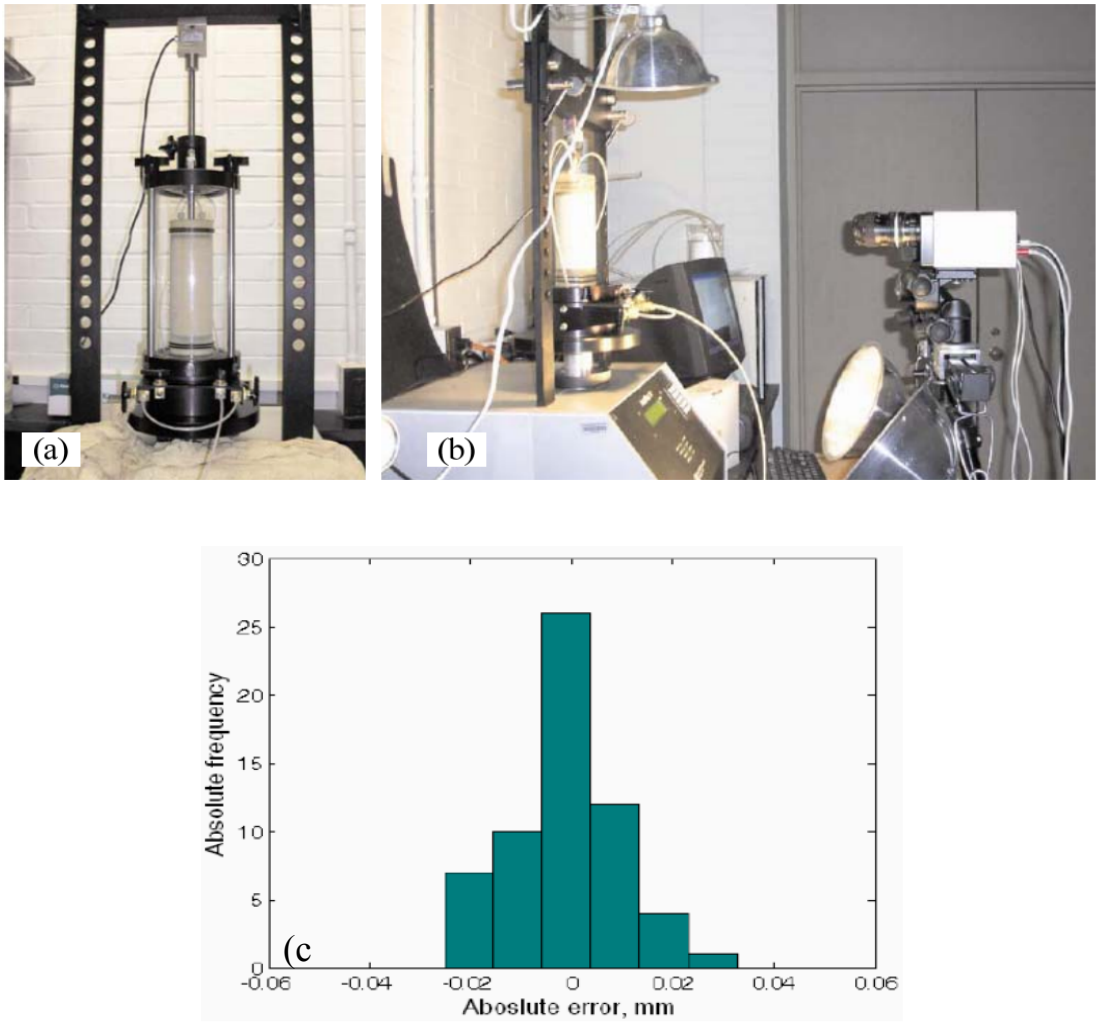


**Figure 2. 2 (a) Geocomp Triaxial setup (b) Geocomp Triaxial and 3D- DIC Setup (c) Absolute error of displacement measurement (Reprinted from Medina, 2006)**

## 2.3 3D-DIC Data Corrections

VIC-3D software is equipped with data corrections for alignment during the calibration. Despite, a slight inclination is observed in the 3D image data plotted on Cartesian coordinate (Song, 2012). Corrections to the 3D image data had been performed previously by determining the best-fit plane through regression analysis of all data points to better align the coordinate system and to correct inclination observed based on plotted image data (Song, 2012). Rotation is performed around the y- axis about an angle of $\theta$ and around the z-axis about an angle of $\varphi$ (Figure 2.4). The rotational angle is determined by relating the normal vector of the best-fit plane with each y and z-axes. Reduced summary of rotational analysis previously performed can be found in table 2.2 and figure 2.3. Based on previous analysis performed by Song (2012), the effect of rotational angle was found to be negligible, thus only translational analysis was performed to correct axis alignment.

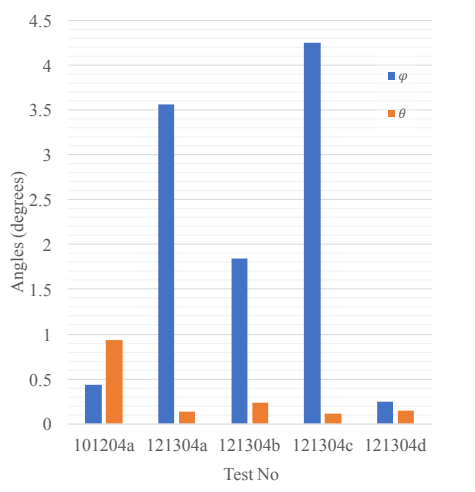


**Figure 2. 3 Histogram of selected case of rotation angle analysis (Reprinted from Medina and Song, 2012)**

**Table 2. 2 Reduced summary of rotation angle analysis (Reprinted from Medina and Song, 2012)**

| | | Angles (degree) | |
|---|---|---|---|
| Test No | TEST ID | $\varphi$ | $\theta$ |
| 11 | 101204a | 0.44021 | 0.93209 |
| 24 | 121304a | 3.56545 | 0.13175 |
| 25 | 121304b | 1.84031 | 0.23194 |
| 26 | 121304c | 4.25209 | 0.10819 |
| 27 | 121304d | 0.24833 | 0.14542 |

The translational transformation was performed to move the origin to the bottom center of the specimen. The origin of raw data points from 3D- DIC is located at the center of the fitting plane. To better align the data coordinates with the physical coordinate system, the data is translated in y and z directions. No translational correction is required in the x- direction. The translation in the y-direction is performed by moving all the data points by 'yb'. 'yb' is determined by determining the distance from the bottom of the specimen to the center of the specimen. Translation in the z- direction was performed to move the corrected best-fit plane from the data domain to the center of the specimen (physical domain). The following process is done by subtracting the average z data values, z_avg, with a threshold of ± 0.02mm from the measured radius shown in Table 2.1. The summary of the translational process can be found in Figure 2.4 (3D) and Figure 2.5 (2D).

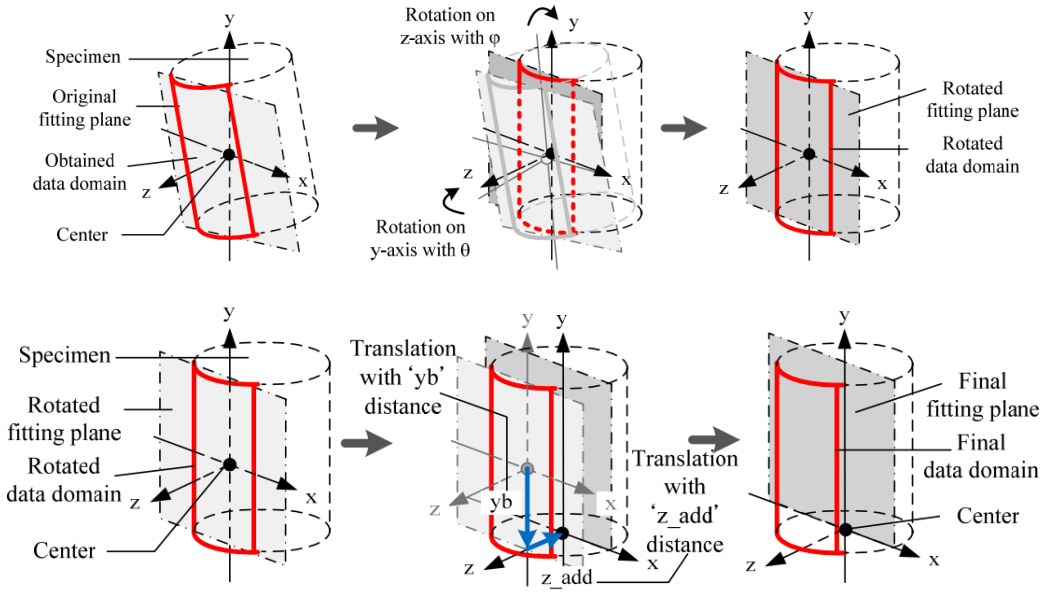


**Figure 2. 4 Correction to tilting observed (Reprinted from Medina and Song, 2012)**

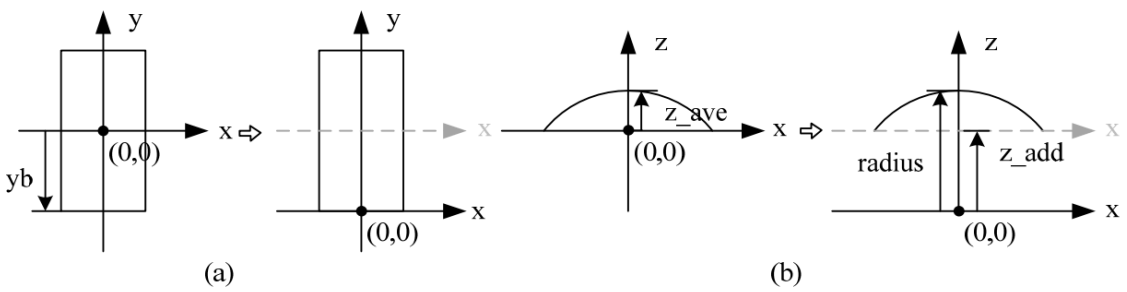


**Figure 2. 5 Alignment of coordinate system (Reprinted from Medina and Song, 2012)**

## 2.4 Cumulative Displacement

As the data processed by VIC-3D is an incremental displacement, adjustments are needed to obtain the cumulative displacement field. To obtain the cumulative displacement, the displacement obtained at the later frames are extrapolated and interpolated into the first frame. The detailed process is shown in figure 2.6, developed by Medina and Song (2012). The first incremental displacement between frame 000 and 004 is by default the cumulative displacement between 0 to 0.2% axial strain levels, figure 2.6 (1). Recall that the reference frame is updated every fourth picture of every 0.2% axial strain. Therefore, to obtain the cumulative displacement between 0 to 0.4% axial strain, the incremental displacement field obtained between frame 004 and 008 (between 0.2% and 0.4% axial strain) is extrapolated and added or interpolated to the first incremental frame, figure 2.6 (3) and (4). This then resulted in the cumulative displacement between the initial/ undeformed frame up to 0.4% axial strain, figure 2.6 (5).

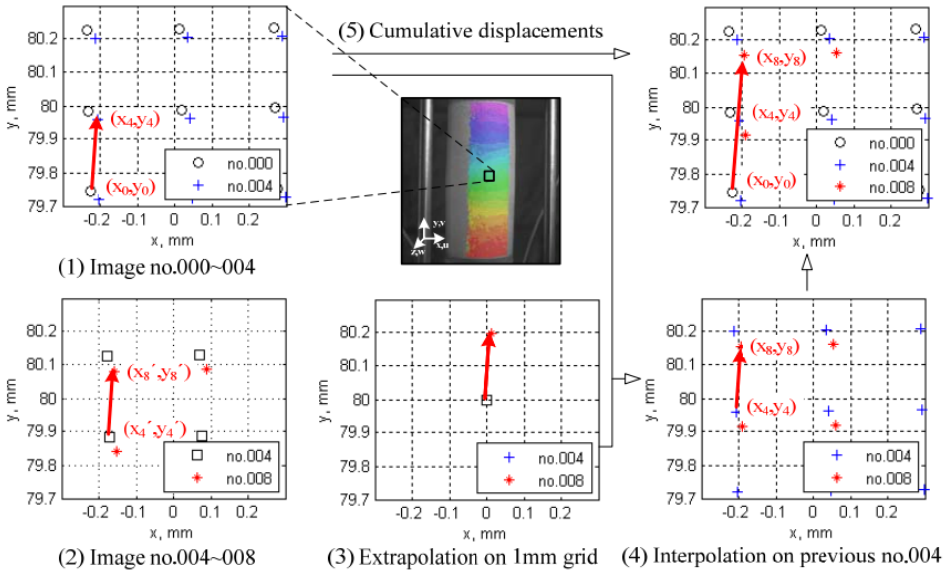


**Figure 2. 6 Interpolation and extrapolation between image no. 000 with no. 008 at 0.4% axial strain step (Reprinted from Medina, 2006 and Song, 2012)**

An additional correction was also made due to the top platen movement, both translation and tilting, observed in early stages during the experiment as shown in figure 3.1 (Medina, 2006). The movement of the top platen is most likely due to local deformation induced by vertical load cell compression, axial loading rod sliding in Plexiglas platen, and soil bedding effect on soil- porous stone interface (Medina, 2006).

The following observation is found consistently in all tests. To correct for this deviation, the global axial strain is computed by taking the difference between the displacement transducer reading located at bottom of specimen with the displacement reading obtained through VIC-3D at top of the specimen. The following phenomenon had also been observed in previous studies by Desrues et al (2010) in which X-Ray μCT and 3D-VOC were utilized to study the onset growth and evolution of localized deformation.

The result based on images obtained by X-ray μCT did not show clear evidence of localized deformation on tilting observed during the experiment.

The corrected data were then investigated prior to being processed for the kinematic analysis. This is performed by randomly checking the displacement field at several points in both global/ material (between first image and image at certain selected axial strain level) and local/ spatial (between two images at different axial strain level) for each experimental data set.

# 3. KINEMATICS ANALYSIS

The study of kinematics deals with motion and how a continuous body deforms without referencing to cause of deformation or motion. The kinematic relationship of a continuum can be defined in terms of its motion and changes to its geometry. Changes to shape or geometry are also known as deformation. Utilizing the 3D- DIC method, the motion or deformation observed on the specimen can be tracked by taking series of pictures taken at various strain level. Recall the experiment is performed at a deformation rate of 0.2% axial strain rate/min. Pictures are taken using a high definition camera every 0.05 % axial strain or every 15 seconds. The following analysis will only consider data up to 12% axial strain as it had been previously noted difficulty arises in tracing the local deformations with respect to undeformed configuration beyond this axial strain level.

## 3.1 Geomechanical Framework

To understand the concept of deformation/ motion, there is a need to introduce the concept of body, configuration, and region. Refer to figure 3.1 to demonstrate the concept of body, configuration, and a region in three-dimensional Euclidian space, $E^3$. Configuration is defined as region of space occupied by a continuum body at a given time, t. The region of space occupied by a body at a certain time can be defined by points and vectors with components in basis $\{e_i\}$, i=1,2,3. Two types of configuration can be defined in the study of kinematics: undeformed (reference) and deformed configuration. The undeformed configuration (Figure 3.1-left) is the initial state of continuum body at time, t=0, where no deformation has been observed. Within this configuration, the region of

space occupied by a body is defined by material points X occupying position or location corresponding to material position vectors $\mathbf{X} = X_i e_i$ relative to the origin (shown in magenta in figure 3.1- left). The coordinate of material point X is defined by $X_i$. The deformed configuration consists of occupied region of space state at current time, t>0 (Figure 3.1- right). The deformed configuration is occupied by spatial point x along with its associated spatial position vectors $\mathbf{x} = x_j e_j$ with respect to the origin. The coordinate spatial point x is defined by $x_j$.

The 3D- DIC results obtained following calibration, post- processing analysis and

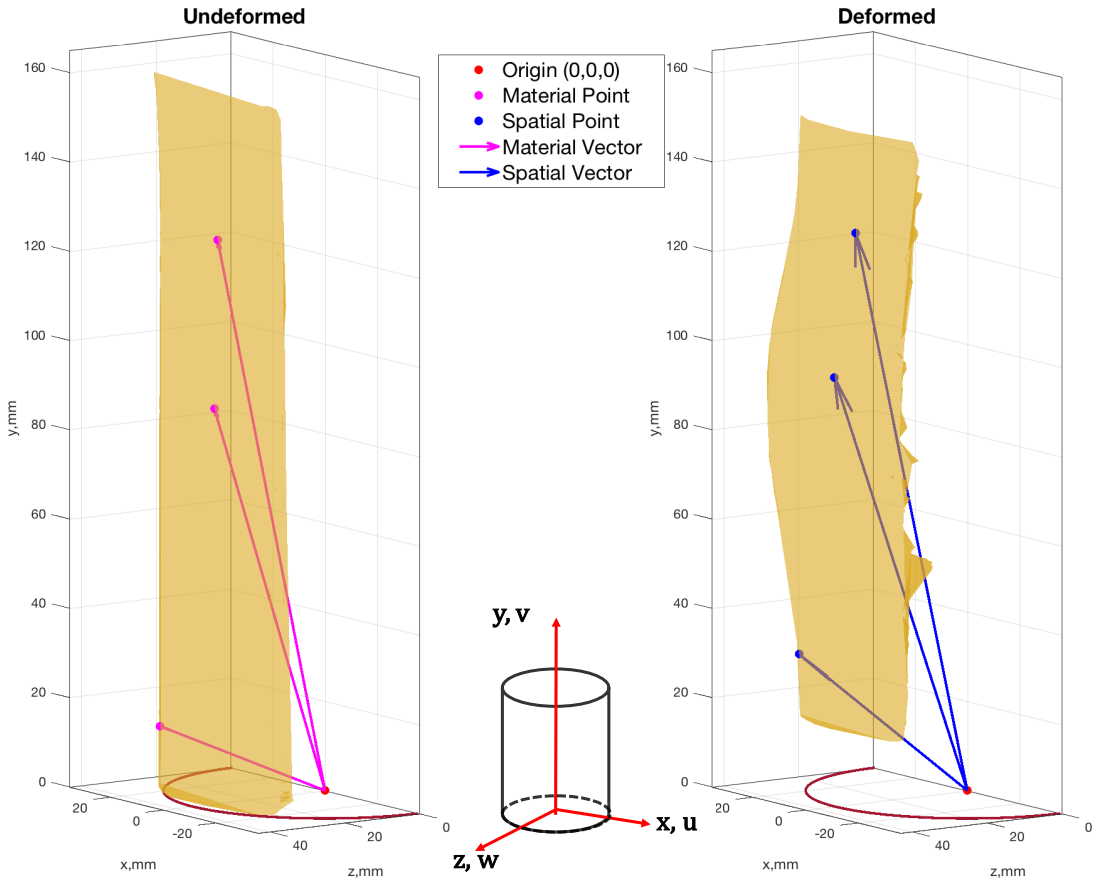


**Figure 3. 1 Test 121304a (40 kPa): (Left) Undeformed/ material configuration at 0% strain; (Right) Deformed/ spatial configuration at 7.2 % strain**

corrections are sets of both material coordinates (Xi) and its corresponding spatial

coordinates (xj). Similar origin will be used in both the deformed and the undeformed configurations in this analysis.

The motion of a body is defined by vector field (collection of vectors), $\chi$, specifying the spatial position of material point X at time t. The motion $\chi$ relates the position of X in undeformed configuration to x, current position of X in the spatial (current) configuration. Thus, the equation of motion can be written as $\mathbf{x} = \chi(\mathbf{X},t)$. The equation of motion is assumed to be uniquely invertible, and consequently, the inverse of the equation of motion can be written as $\mathbf{X} = \chi^{-1}(\mathbf{x},t)$.

### *3.1.1 Descriptions*

In studying the motion and deformation of a body, the evolution of a body with respect to time can be defined based on a selected reference configuration. The reference configuration is the configuration to which state variables such as stress, strain, and displacement are referred (Mathisen, 2012). In Lagrangian (material) description, the state variables are expressed in terms of time and its initial (material) configuration. Similarly, when the spatial points are used as the reference configuration then the deformation/ motion is observed in the spatial or Eulerian description. In finite element, these descriptions may also be referred as mesh where the nodes are the reference coordinates being fixed during the motion (Belytschko, 2000).

The Langrarian description has been widely used in the study of solid mechanics. In the Lagrangian description, an observer tracked changes to material points position and physical properties as time progresses and material points occupies undeformed

configuration (Banks et al, 2011). The nodes of Lagrangian mesh are coincident with the material point. As the body deforms, the nodes and material points changes position but the relative position between the material points and the nodes remains fixed. The equation of motion in Lagrangian description has been previously defined as $\mathbf{x} = \chi(\mathbf{X},t)$. The measurement of state variable in Lagrangian description is in terms of total measure, i.e. total measure of strain.

The motion in Eulerian (spatial) description is described in terms of current (spatial) configuration. In the Eulerian description, changes to material points in space is observed in the current configuration as time progresses (Banks et al, 2010). Therefore, the nodes in Eulerian mesh are coincident with the spatial points while material points can move during motion. The following approach is used mostly in the study of fluid mechanics where difficulty arises in defining reference configuration. Particles are treated as a continuum thus, the corresponding balance law is assumed in a control volume basis (Zhang et al, 2007). The equation of motion in Eulerian Description has previously been defined as the inverse of equation of motion $\mathbf{X} = \chi^{-1}(\mathbf{x},t)$.

Similar results are obtained in both Lagrangian and Eulerian approach. However, severe mesh distortion had been observed in several studies when performing large deformation analysis (Nazdem et al, 2010; Liyanapathirana, 2009). The divergence of

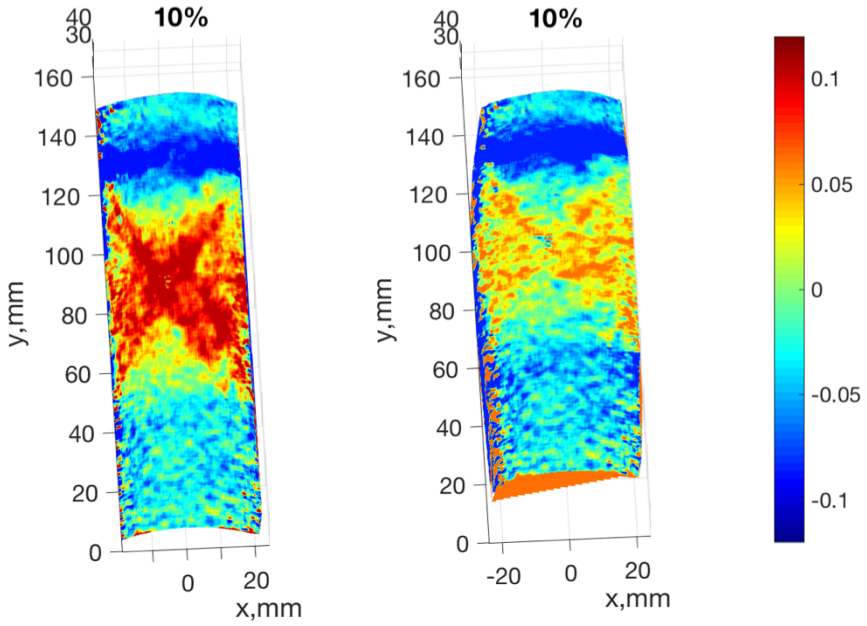


**Figure 3. 2 Tests 121304c (60 kPa): Divergence at 10% axial strain in Lagrangian (left) and (Eulerian (right) descriptions**

displacement in Lagrangian and Eulerian description observed at 10% axial strain for test 121304c (60 kPa) is presented in figure 3.2.

To accommodate the limitations observed in both Lagrangian and Eulerian description, Updated Lagrangian (UL) and Arbitrarily Lagrangian Eulerian (ALE) methods had been implemented in several studies. Updated Lagrangian had been applied to accommodate analysis where constitutive equations are expressed in rate form. To accommodate the limitation, Borja and Alarcon (1995) introduced the concept of multiplicative decomposition of deformation gradient to study elasto- plastic consolidation of fully saturated soil. UL method is also applicable in analyzing liquefiable soil. The initial configuration is updated continuously in the UL method. In addition, ALE has also been applied to study large deformation in soils (Liyanapathirana, 2009; Nazem

et al, 2007). The ALE method is typically applied to analyze coupled solid mechanics phenomenon.

### *3.1.2 Data Implementation*

The corrected data sets available for each picture are equipped with the information of the spatial points along with its corresponding material points. The first picture in the data set provides the undeformed configuration information. To track the material points as the sample deforms, common material coordinates between two pictures are identified using developed MATLAB algorithm. As the sample is loaded, reduction in material points is observed thus, least amount of material points remains on the last picture or highest axial strain level in the analysis.

If the reference point at earlier strain level is found in the later dataset, it can be concluded that the point is traceable, thus displacement can be obtained. It had been observed that some points disappeared and new points appeared due to compression, dilation, and rotation observed along the specimen boundary. As the sample is loaded, new points are introduced within the middle section of the specimen where bulging is observed. Missing coordinates are observed along the lower portion of the specimen as the specimen is compressed (sample is loaded from the bottom with up direction) and decrease in height. As the sample is loaded from the bottom, the majority of coordinates missing should be in the lower portion of the sample.

The reference point in each image is defined by x, y, and z coordinates. The corresponding displaced/ spatial points is defined for each reference point as xm, ym, zm.

The global cumulative displacement can then be obtained by subtracting the displaced coordinate with the reference coordinate. The data is then compared with the global cumulative displacement recorded in each deformed data set, specified as dx, dy, dz). The incremental displacement is obtained by comparing the difference of current incremental displacement with the difference of spatial coordinate between two pictures. Based on the analysis performed, the results between the two different approaches to obtain incremental displacement matches.

### *3.1.3 Displacement Fields*

The displacement of a point can be defined by a vector. The changes in position of a point along the surface boundary of sand specimen can be tracked during the test utilizing 3D-DIC method. The changes in position of the points are defined by displacement vectors where the collection of these vectors along a surface or within a volume is known as vector field. The concept of vector field will be used to observe the displacement along the sand specimen surface based on pictures collected during testing.

The displacement field is a vector field which defines deformation/ changes in shape of a continuum body. The displacement field is composed of multiple displacement vectors. Boundary information defined by the material and spatial coordinates captured during the testing by HD camera can be utilized to define displacement field. Displacement vector is the vector defining how body deform from current configuration to another configuration. The displacement field can be obtained in the Langrarian description or Eulerian description. In Lagrangian description, the displacements of each

material points are describe in terms of the change in position of spatial point, $\boldsymbol{x}(\boldsymbol{X}, t)$, at time t>0 with respect to the associated material point , $\boldsymbol{X}$, at initial undeformed (reference) configuration. The displacement of each point is decribed by a vector $\boldsymbol{U}(\boldsymbol{X}, t)$, connecting the material point with the spatial point at time t. The displacement in Lagrangian description is presented in equation 3.1. The spatial displacement is the change in position of material point, $\boldsymbol{X}(\boldsymbol{x}, t)$, with respect to fixed spatial point, $\boldsymbol{x}$, as reference. The displacement in Eulerian description, $\boldsymbol{u}(\boldsymbol{x}, t)$, is presented in equation (3.2).

$$\text{Displacement in material description : } \boldsymbol{U}(\boldsymbol{X}, t) = \boldsymbol{x}(\boldsymbol{X}, t) - \boldsymbol{X} \quad (3.1)$$

$$\text{Displacement in spatial description : } \boldsymbol{u}(\boldsymbol{x}, t) = \boldsymbol{x} - \boldsymbol{X}(\boldsymbol{x}, t) \quad (3.2)$$

The displacements of the material and spatial points at different strain levels were determined utilizing MATLAB. Graphical presentation of the Lagrangian (material) displacement in each direction is presented in Figure 3.3. Graphical representation of the Eulerian (spatial) displacement is presented in figure Figure 3.4. The displacement is observed at 0.4% axial strain step in the analysis.

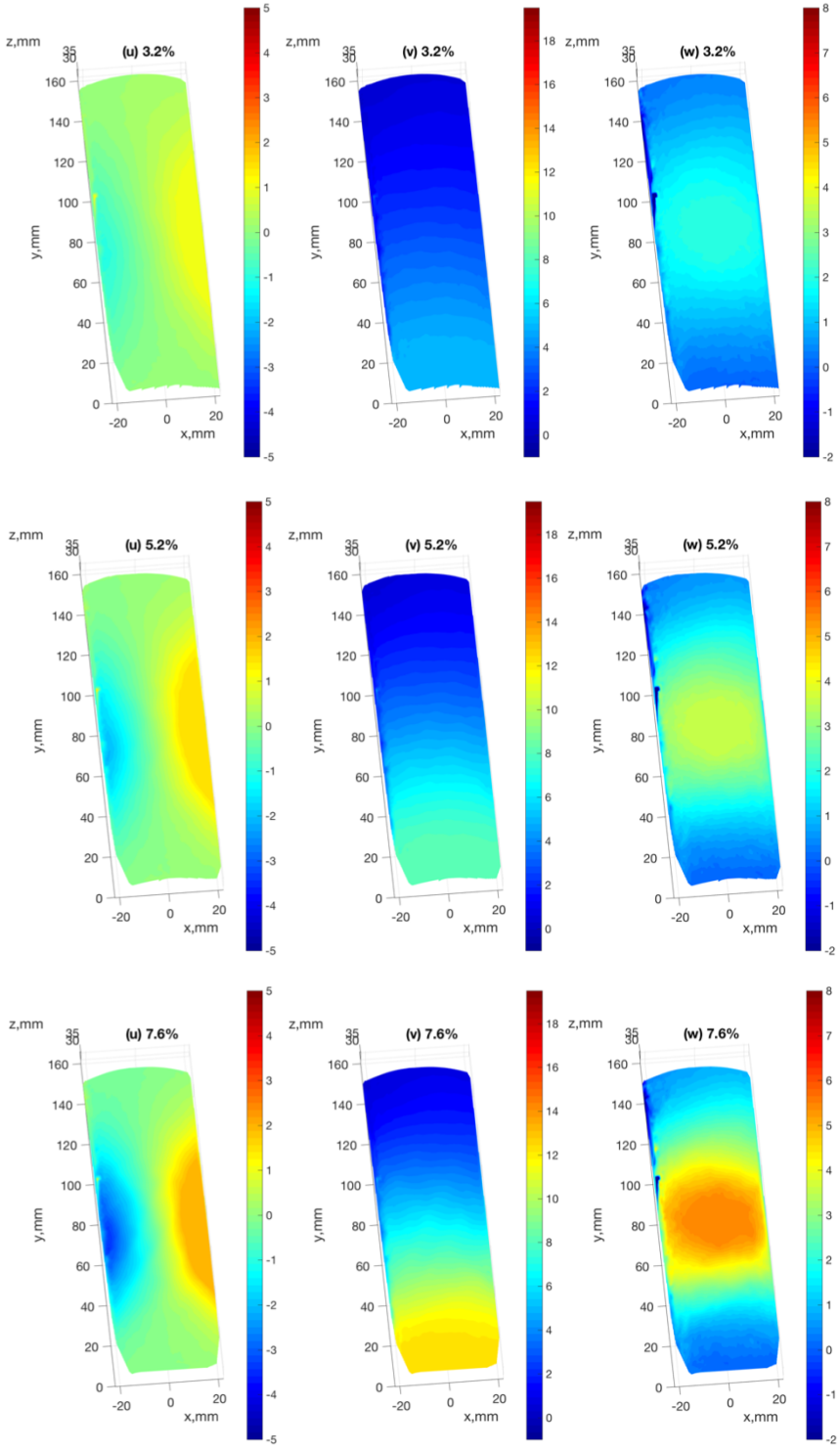


**Figure 3. 3 Test 121304d (20kPa) Lagrangian Displacement at 3.6%, 5.2%, and 7.2% axial strain. (Left) Material displacement in x- direction. (Middle) Material Displacement in y-direction. (Right) Material Displacement in z- direction.**

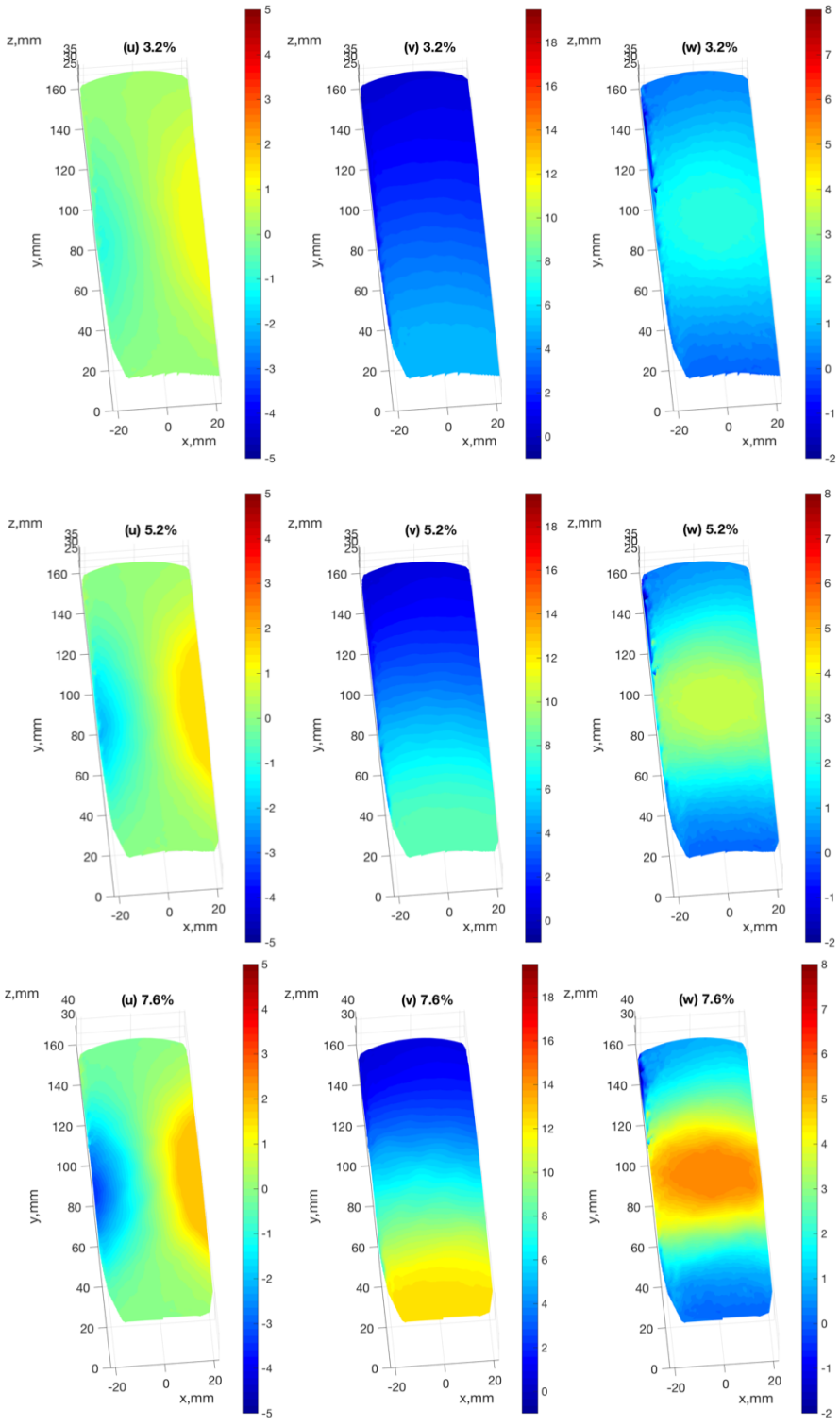


**Figure 3. 4 Test 121304d (20kPa) Eulerian Displacement at 3.6%, 5.2%, and 7.2% axial strain. (Left) Material displacement in x- direction. (Middle) Material Displacement in y-direction. (Right) Material Displacement in z- direction.**

As bulging is observed along the middle of the sample and the sample is compressed, most displacements are observed in the radial and vertical displacement. Therefore, to consider these observations, we can obtain the displacement in the cylindrical coordinate system.

To obtain the displacement in the cylindrical coordinate system, the data provided in cartesian system is first converted into cylindrical coordinates system (Figure 3.5). Vectors in cylindrical coordinate system is defined by its length projected onto the x-z plane, angular direction from the x- axis and vertical distance away from the origin. The length of the vector (r) can be determined by determining the projected magnitude of the material or spatial vector on x-z plane. This definition is similar to the definition of the radius of the specimen at point of interest.

The angular direction of the vector ($\theta$) is determined by determining the angle between the x and z component of the vector or x and y in MATLAB cartesian coordinate system. Positive angular vector ($\theta$) is in counter- clockwise direction. The vertical distance of the vector (z) is similar to the y- coordinate in cartesian form. Thus, the cylindrical coordinate system is written as (r, $\theta$, z). Detailed coordinate conversion is presented in Table 3.1. MATLAB command cart2pol is used in the analysis to convert from cartesian to cylindrical coordinate system.

**Table 3. 1 Cartesian to cylindrical coordinate system conversion**

| MATLAB Cylindrical | DATA CARTESIAN | CONVERSION |
|---|---|---|
| (r, $\theta$, z) | (x,z,y) | $r = \sqrt{x^2 + z^2}$ |
| (dr, d$\theta$, dz) | (dx,dz,dy) | $\theta = \tan^{-1}(\frac{z}{x})$ |
| | | $z = y$ |

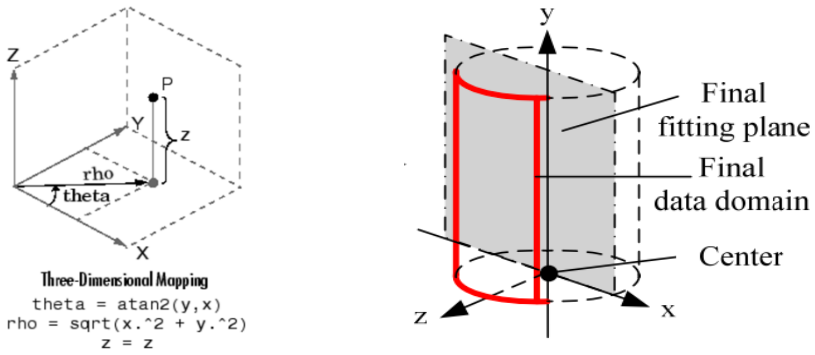


**Figure 3. 5 (Left) Cylindrical coordinate system in MATLAB (MATLAB, 2017) (Right) Cartesian coordinate system used in analysis (Reprinted from Song, 2012)**

The displacements in cylindrical coordinate can be determined similarly to the cartesian coordinate system. Equation 3.1 and 3.2 are used to determine the changes in the cylindrical coordinate system. The changes observed in vertical direction in cylindrical coordinate system is similar to those obtained in cartesian coordinate system. The graphical presentation of material and spatial displacement fields in cylindrical coordinate will be presented in section 4.2**.**

## 3.2 Kinematic Operators

The deformation of a body is defined by the mapping of motion or deformation from the undeformed configuration to the deformed configuration. The mapping of deformation is related by deformation gradient tensor, **F.** In understanding the deformation of the body, there's also a need to define some kinematic operators such as divergence of displacement fields, and curl of displacement fields.

### *3.2.1 Divergence and Curl*

The divergence of a vector field represents how much sink and source is observed at a point. Thus, the divergence of the displacement field can be defined as expansion or compression observed on the surface of the sample. A positive divergence signifies increase in soil mass per unit volume (expansion) under applied load. Convergence or compression occurred when the divergence is negative and zero divergence correlates to no source or sink at a given point. Divergence can be performed in material configuration (3.3) or spatial configuration (3.4).

Material Divergence (2D): $\nabla \cdot \boldsymbol{U} = div\, \boldsymbol{U} = \frac{\partial U_1}{\partial X_1} + \frac{\partial U_2}{\partial X_2}$ (3.3a)

Material Divergence (3D): $\nabla \cdot \boldsymbol{U} = div\, \boldsymbol{U} = \frac{\partial U_1}{\partial X_1} + \frac{\partial U_2}{\partial X_2} + \frac{\partial_3}{\partial X_3}$ (3.3b)

Spatial Divergence (2D): $\nabla \cdot \boldsymbol{u} = div\, \boldsymbol{u} = \frac{\partial u_1}{\partial x_1} + \frac{\partial u_2}{\partial x_2}$ (3.4a)

Spatial Divergence (3D): $\nabla \cdot \boldsymbol{u} = div\, \boldsymbol{u} = \frac{\partial u_1}{\partial x_1} + \frac{\partial u_2}{\partial x_2} + \frac{\partial u_3}{\partial x_3}$ (3.4b)

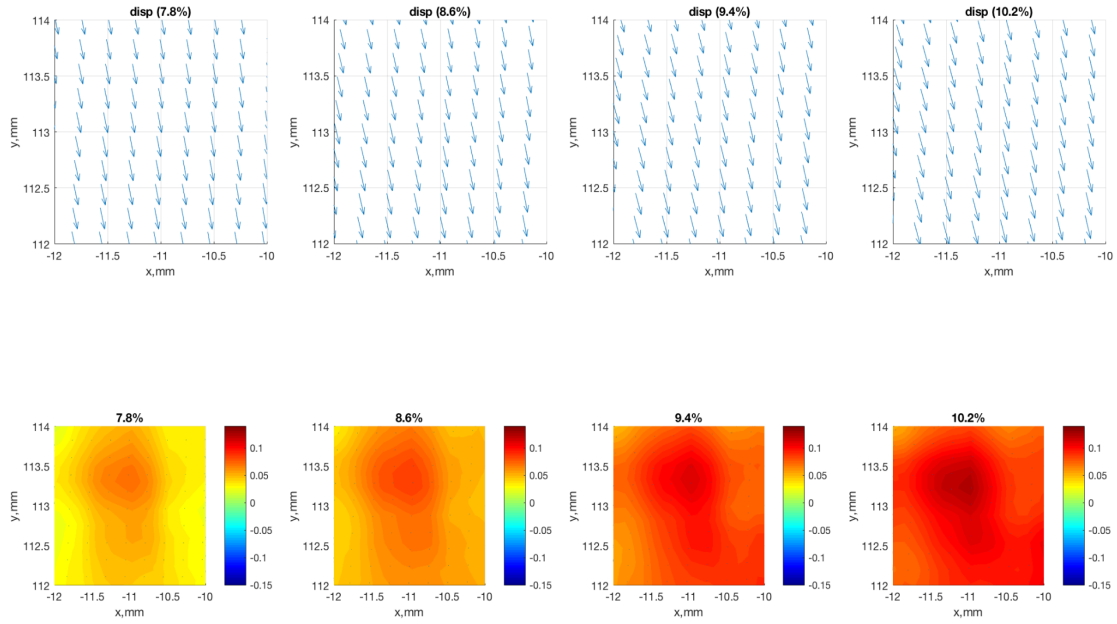


**Figure 3. 6 Test 121304a Material divergence subsets at 7.8%, 8.8%, 9.4%, and 10.2%**

The curl operator defines how much rotation is observed at a point. When the curl is zero, no rotation will be observed. Positive curl corresponds to counter- clockwise rotation while negative curl corresponds to clockwise rotation.

Material Curl (2D): $$\nabla \times \boldsymbol{U} = curl\ \boldsymbol{U} = \frac{\partial U_2}{\partial X_1} - \frac{\partial U_1}{\partial X_2} \tag{3.5a}$$

Material Curl (3D): $$\nabla \times \boldsymbol{U} = curl\ \boldsymbol{U}$$

$$\nabla \times \boldsymbol{U} = \left(\frac{\partial U_3}{\partial X_2} - \frac{\partial U_2}{\partial X_3}\right) e_1 + \left(\frac{\partial U_1}{\partial X_3} - \frac{\partial U_3}{\partial X_1}\right) e_2 + \left(\frac{\partial U_2}{\partial X_1} - \frac{\partial U_1}{\partial X_2}\right) e_3 \tag{3.5b}$$

Spatial Curl (2D): $$\nabla \times \boldsymbol{u} = curl\ \boldsymbol{u} = \frac{\partial u_2}{\partial x_1} - \frac{\partial u_1}{\partial x_2} \tag{3.6a}$$

Spatial Curl (3D):

$$\nabla \times \boldsymbol{u} = curl\ \boldsymbol{u}$$

$$\nabla \times \boldsymbol{u} = \left(\frac{\partial u_3}{\partial x_2} - \frac{\partial u_2}{\partial x_3}\right) e_1 + \left(\frac{\partial u_1}{\partial x_3} - \frac{\partial u_3}{\partial x_1}\right) e_2 + \left(\frac{\partial u_2}{\partial x_1} - \frac{\partial u_1}{\partial x_2}\right) e_3 \qquad (3.6b)$$

An example of material divergence and spatial curl are presented in figure 3.6 and 3.7 respectively. The following analysis will only consider 2D divergence and curl observed in the x-y direction. It is possible to perform the analysis in 3D; however, high computing time is needed to perform the operation.

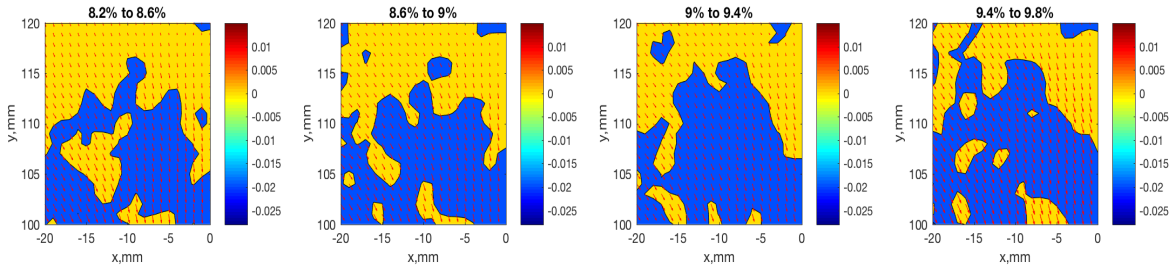


**Figure 3. 7 Test 121304a Material curl subsets at 8.2 to 8.6%, 8.6 to 9%, 9 to 9.4%, and 9.4 to 9.8% axial strain**

### *3.2.2 Gradient*

The gradient of a vector field defines the translational and rotational rate of change. The gradient of displacement field also defines the stretches, changes in volume, and rotation is observed at a point. The gradient of displacement field or deformation gradient is a tensor [**F**] which defines a mapping of infinitesimal material 'fiber' from the initial configuration to the spatial configuration (Geilo, 2012). [**F**] is a Jacobian matrix of motion

$\chi$ ($\mathbf{X_i}$,t). The mapping of the initial material fiber into spatial configuration is defined by the motion of its neighboring particles.

The material fibers are defined by the material, spatial points and the corresponding elemental vectors. As a body deforms, the mapping of a material point to the deformed configuration can be described by position vectors or elemental vectors with respect to the surrounding points. A subset of undeformed and deformed configuration is presented in figure 3.8. In the initial configuration, the material points P (point 15001), $Q_1$ (point 15002), and $Q_2$ (point 15323) has deformed to current spatial positions p, $q_1$, and $q_2$

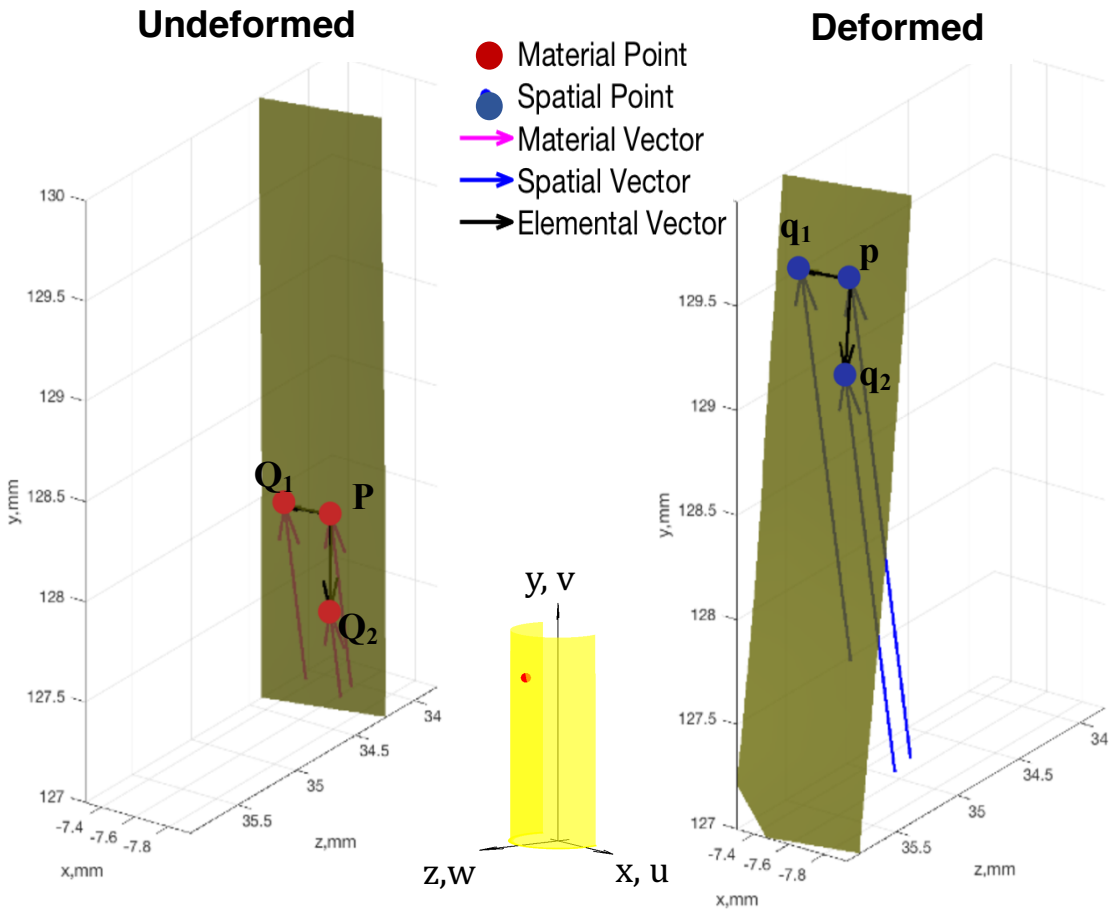


**Figure 3. 8 Test 121304c:Subset of points 15001 , 15002, and 15323 at undeformed configuration (0% axial strain) and 11.2% axial strain.**

respectively. The motion of the material points into the undeformed configuration is defined by $\mathbf{x_i} = \chi\ (\mathbf{X_i}, t)$. The position of points $Q_1$ and $Q_2$ relative to point P are defined by elemental vector or infinitesimal line segment $d\mathbf{X_j}$, where $d\boldsymbol{X_1} = \boldsymbol{X_{Q_1}} - \boldsymbol{X_P}$ and $d\boldsymbol{X_2} = \boldsymbol{X_{Q_2}} - \boldsymbol{X_P}$. In the undeformed configuration, the corresponding elemental vector is $d\mathbf{x_j}$, where $d\boldsymbol{x_1} = \boldsymbol{x_{q_1}} - \boldsymbol{x_P}$ and $d\boldsymbol{x_2} = \boldsymbol{x_{q_2}} - \boldsymbol{x_P}$. In the material description, the spatial elemental vector can be written as $d\boldsymbol{x_1} = \chi\ (\boldsymbol{X_P}. + d\boldsymbol{X_1}, t) - \chi\ (\boldsymbol{X_P}, t)$ and $d\boldsymbol{x_2} = \chi\ (\boldsymbol{X_P}. + d\boldsymbol{X_2}, t) - \chi\ (\boldsymbol{X_P}, t)$. The deformation gradient or gradient of displacement, which describes how much stretch and rotations observed, can then be defined as presented in equations 3.7 and 3.8.

Material Deformation Gradient (2D):

$$grad\ \mathbf{U} = \boldsymbol{\nabla}\ \mathbf{U} = \boldsymbol{\nabla}\ \otimes \mathbf{U} = \begin{bmatrix} \frac{\partial U_1}{\partial X_1} & \frac{\partial U_1}{\partial X_2} \\ \frac{\partial U_2}{\partial X_1} & \frac{\partial U_2}{\partial X_1} \end{bmatrix} \tag{3.7a}$$

Material Deformation Gradient (3D):

$$grad\ \mathbf{U} = \boldsymbol{\nabla}\ \mathbf{U} = \boldsymbol{\nabla}\ \otimes \mathbf{U} = \begin{bmatrix} \frac{\partial U_1}{\partial X_1} & \frac{\partial U_1}{\partial X_2} & \frac{\partial U_1}{\partial X_3} \\ \frac{\partial U_2}{\partial X_1} & \frac{\partial U_2}{\partial X_1} & \frac{\partial U_2}{\partial X_3} \\ \frac{\partial U_3}{\partial X_1} & \frac{\partial U_3}{\partial X_1} & \frac{\partial U_3}{\partial X_3} \end{bmatrix} \tag{3.7b}$$

Spatial Deformation Gradient (2D):

$$grad\,\mathbf{u} = \boldsymbol{\nabla}\,\mathbf{u} = \boldsymbol{\nabla} \otimes \mathbf{u} = \begin{bmatrix} \frac{\partial u_1}{\partial x_1} & \frac{\partial u_1}{\partial x_2} \\ \frac{\partial u_2}{\partial x_1} & \frac{\partial u_2}{\partial x_2} \end{bmatrix} \tag{3.8a}$$

Spatial Deformation Gradient (3D):

$$grad\,\mathbf{u} = \boldsymbol{\nabla}\,\mathbf{u} = \boldsymbol{\nabla} \otimes \mathbf{u} = \begin{bmatrix} \frac{\partial u_1}{\partial x_1} & \frac{\partial u_1}{\partial x_2} & \frac{\partial u_1}{\partial x_3} \\ \frac{\partial u_2}{\partial x_1} & \frac{\partial u_2}{\partial x_2} & \frac{\partial u_2}{\partial x_3} \\ \frac{\partial u_3}{\partial x_1} & \frac{\partial u_3}{\partial x_2} & \frac{\partial u_3}{\partial x_3} \end{bmatrix} \tag{3.8b}$$

# 4. MATLAB IMPLEMENTATION

The results of qualitative analysis of deformation kinematics described in the previous chapter will be discussed in the following section. MATLAB algorithm is utilized to apply the kinematic operators. A comparison will be drawn with localization observed in the digital images obtained through 3D- DIC technique.

## 4.1 Summary of Missing Points

Summary of missing points analysis in the spatial description with 0.8% axial strain difference between frames is presented in Figure 4.1 for all tests. The associated stress- strain curve has been previously presented in Figure 2.1. The number of spatial points reduces as the sample is loaded. For all tests, the distribution of number of missing points initially increases up to approximately 2 % axial strain. The number of missing points then decreases with periodic increase in number beyond 2% axial strain. The peak maximum is observed later for the 20 kPa confining sample. Minimum percentage of missing points is observed at 7.6 to 8.4% axial strain. Based on this observation, it can be concluded that most compression occurs in in earlier strain, approximately below 3% axial strain.

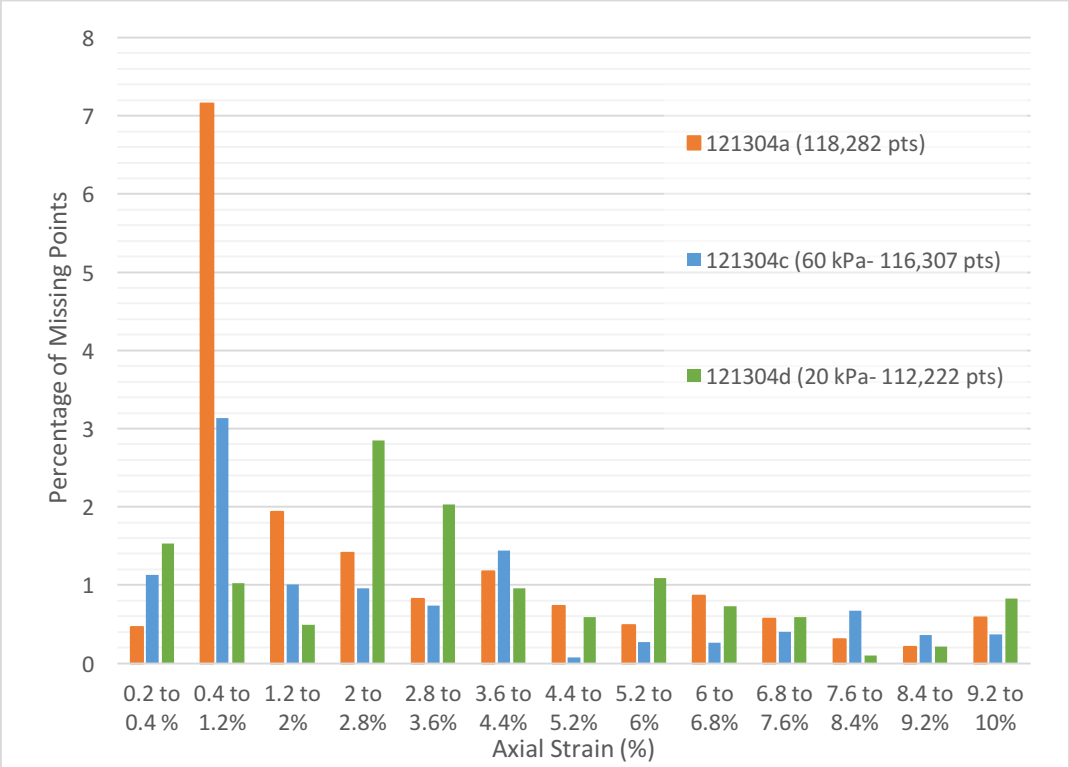


**Figure 4. 1 Percentage of missing spatial points for all tests in spatial description with 0.8 % axial strain step**

## 4.2 Displacement Fields

Displacement fields at selected strain rate for tests 121304d (20 kPa), 121304a (40 kPa), and 121304c (60 kPa) are shown in figure 3.3, 3.4, and 4.2 to 4.7 for cartesian system and 4.9 to 4.14 for cylindrical system.

### *4.2.1 Cartesian Displacement Fields*

In the Cartesian system, the displacement in x- direction is observed mostly in the mid-edges part of the sample. The displacement observed along the top, bottom, and mid-center part of the sample in x- direction is minimal to none. The magnitude of displacement observed is highest at the edges and decreases towards the center of the

specimen. Therefore, it can be concluded the sample is bulging outward in the x- direction. It has also been observed where the magnitude of material displacement is zero in the x-direction, displacement is observed in y- and z- direction, with exception to the top of the sample.

In the y-direction, minimal to zero displacement is observed along the top of the sample, signifying sample is restrained at the top as loading progresses. Reduction in height at the top of the sample has been addressed in Section 2 related to observed top platen movement. Similar displacement bands developed at the lower strain. The intermediate band started to develop prior to maximum strain. Within the strain softening range, the specimen separated into three sections, high displacement region observed at bottom of sample, intermediate displacement region along the middle of the sample and minimal to no displacement region along the top of the sample. Highest displacement is observed at the bottom of the sample as the sample move upwards. Narrower intermediate zone is observed in loose and low confining pressure specimens. Small to no intermediate region is observed in sample loaded.

Some pattern of inclination within the intermediate zone, developed during the softening region and become consistent towards the end of softening. V- shape pattern is observed to developed starting the beginning of softening which is also observed by Rechenmacher (2005). This pattern appears to develop into the shear band as seen clearly in 121304c (60 kPa) specimen at the higher strain. The pattern is not clearly observed in the loose specimen.

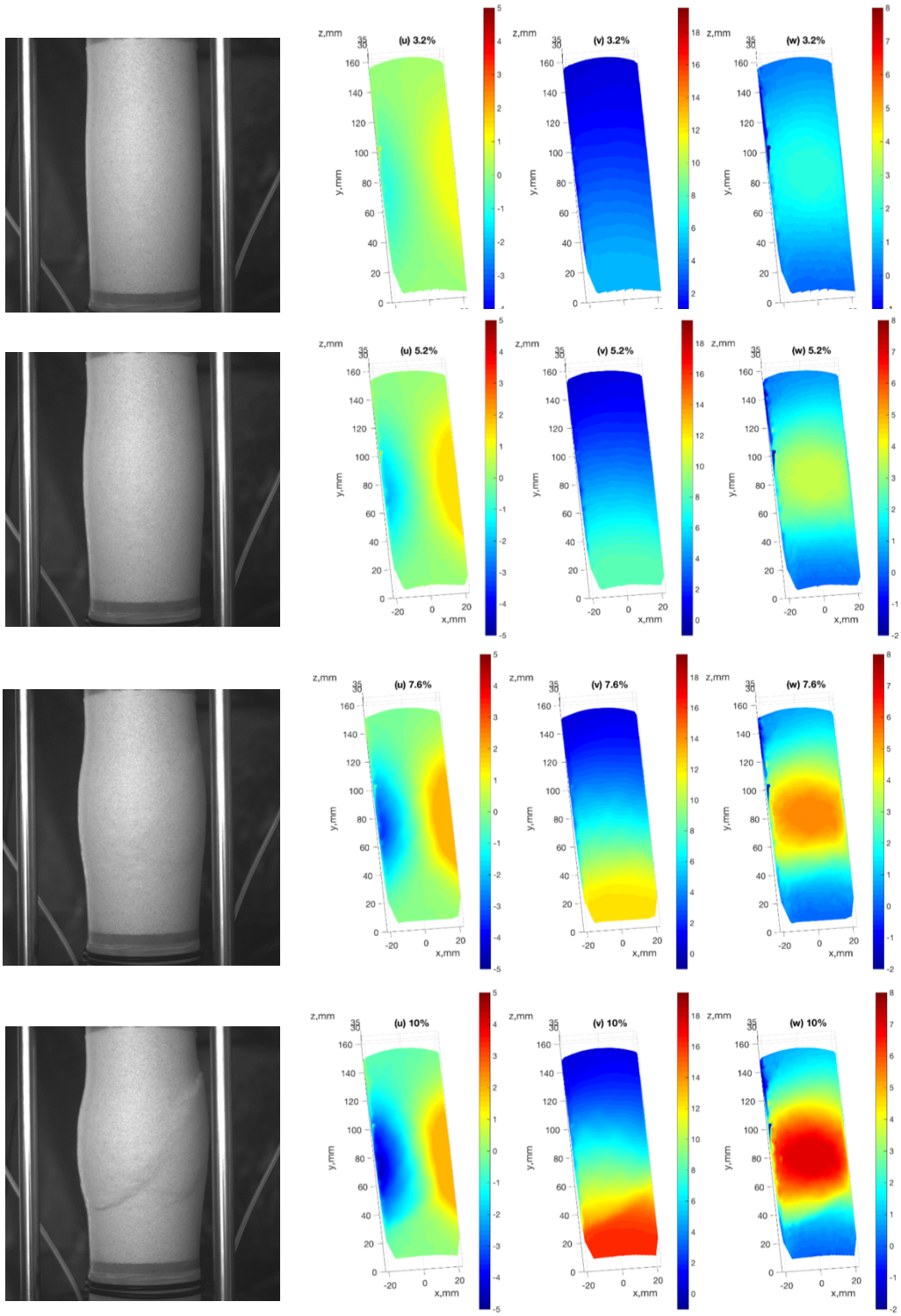


**Figure 4. 2 Test 121304d (20 kPa)- Picture of digital images (Medina, 2006) and plot of Displacement (cartesian) in Lagrangian Description at 3. 2%, 5.6%, 7.2%, and 10% axial strain. (Left) x- direction, (Middle) y- direction, (Right) z-direction.**

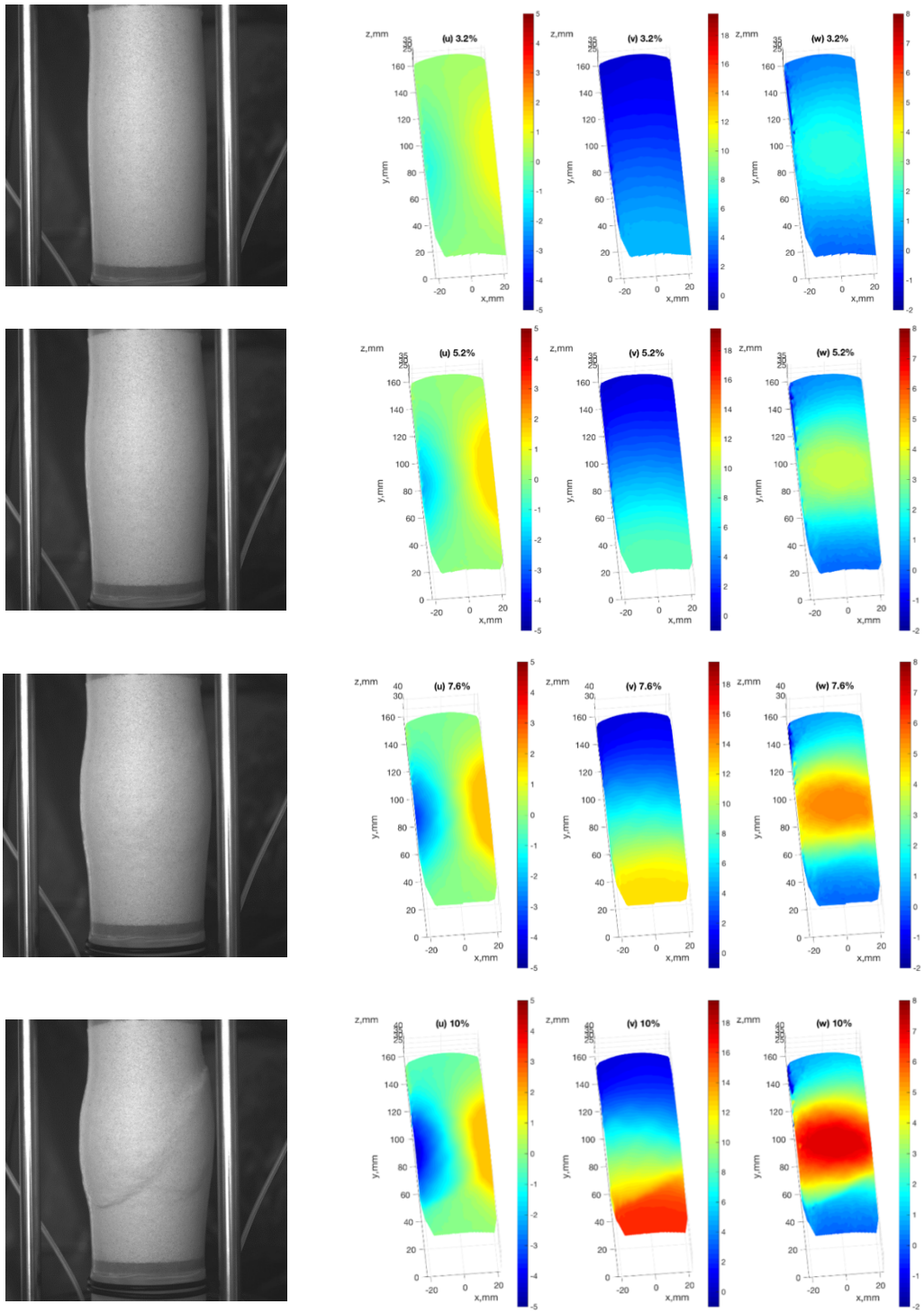


**Figure 4. 3 Test 121304d (20 kPa)- Picture of digital images and plot of Displacement (cartesian) in Eulerian Description at 3. 2%, 5.6%, 7.2%, and 10% axial strain. (Left) x-direction, (Middle) y- direction, (Right) z-direction.**

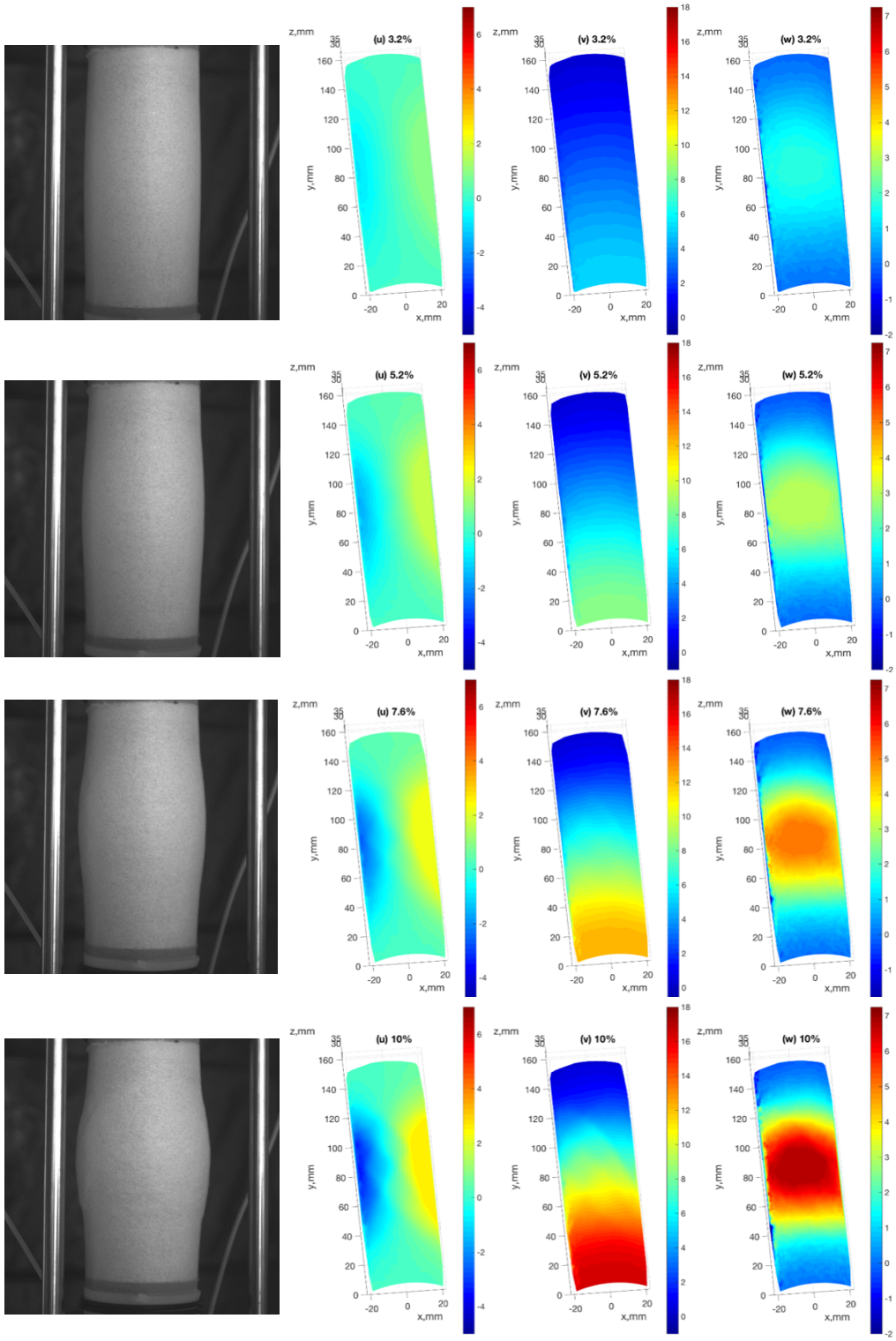


**Figure 4. 4 Test 121304a (40 kPa)- Picture of digital images (Medina, 2006) and plot of Displacement (cartesian) in Lagrangian Description at 3. 2%, 5.2%, 7.2%, and 10% axial strain. (Left) x- direction, (Middle) y- direction, (Right) z-direction.**

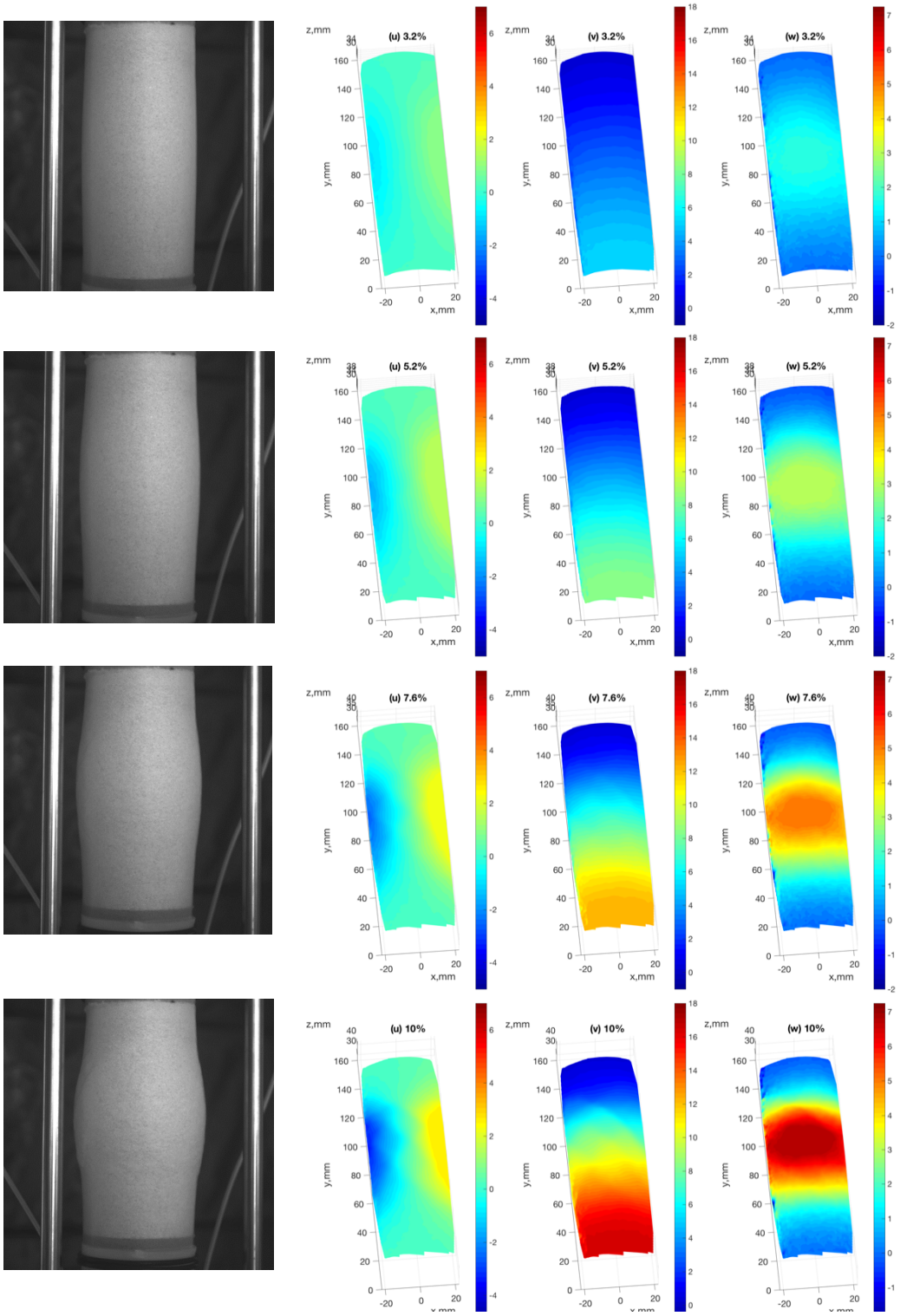


**Figure 4. 5 Test 121304a (40 kPa)- Picture of digital images (Medina, 2006) and plot of Displacement (cartesian) in Eulerian Description at 3. 2%, 5.2%, 7.2%, and 10% axial strain. (Left) x- direction, (Middle) y- direction, (Right) z-direction.**

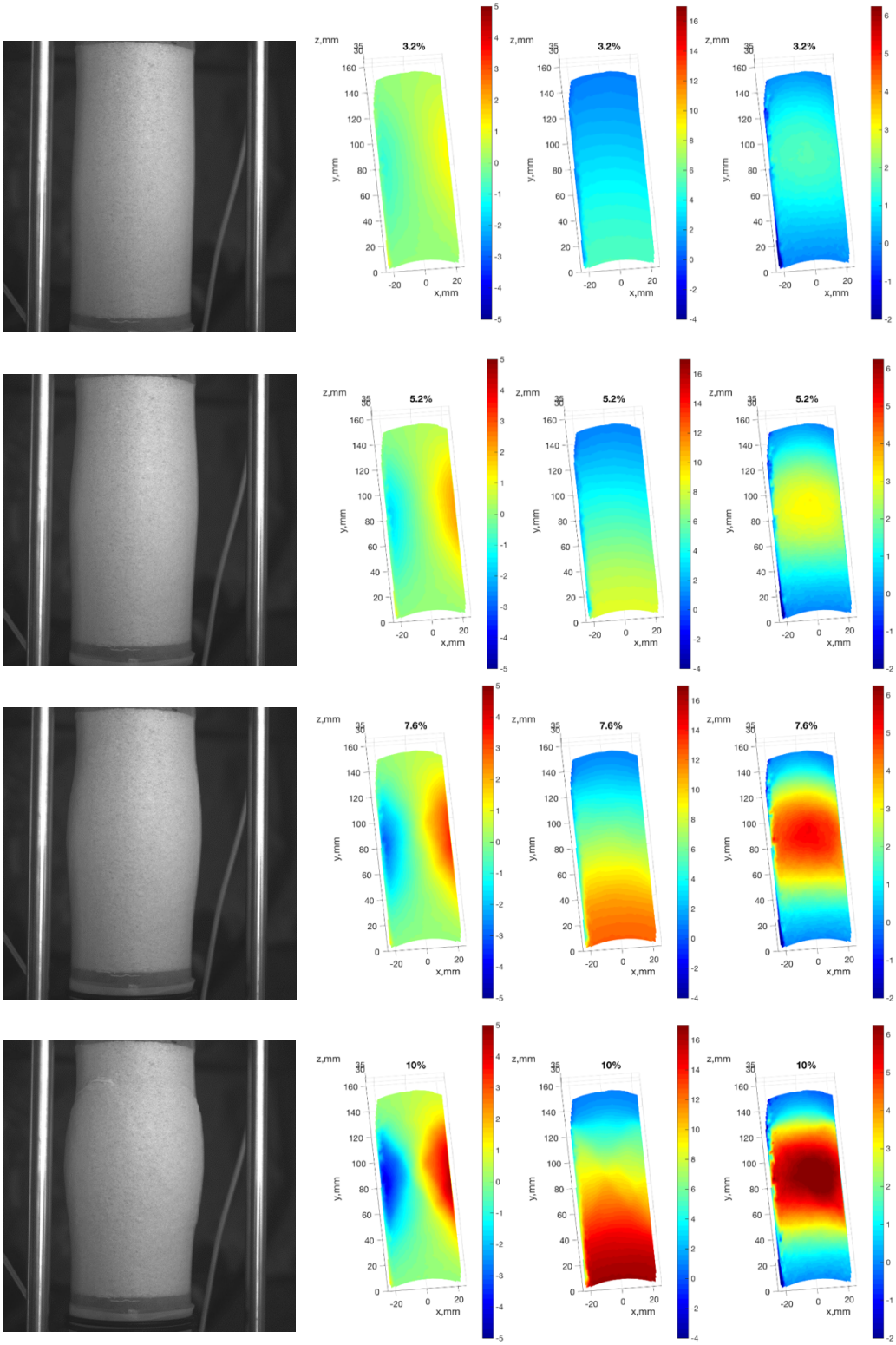


**Figure 4. 6 Test 121304c- Digital Images (Medina, 2006) and Displacement (cartesian) in Lagrangian Description at 3. 2%, 5.2%, 7.2% and 10% axial strain. (Left) x- direction, (Middle) y- direction, (Right) z-direction.**

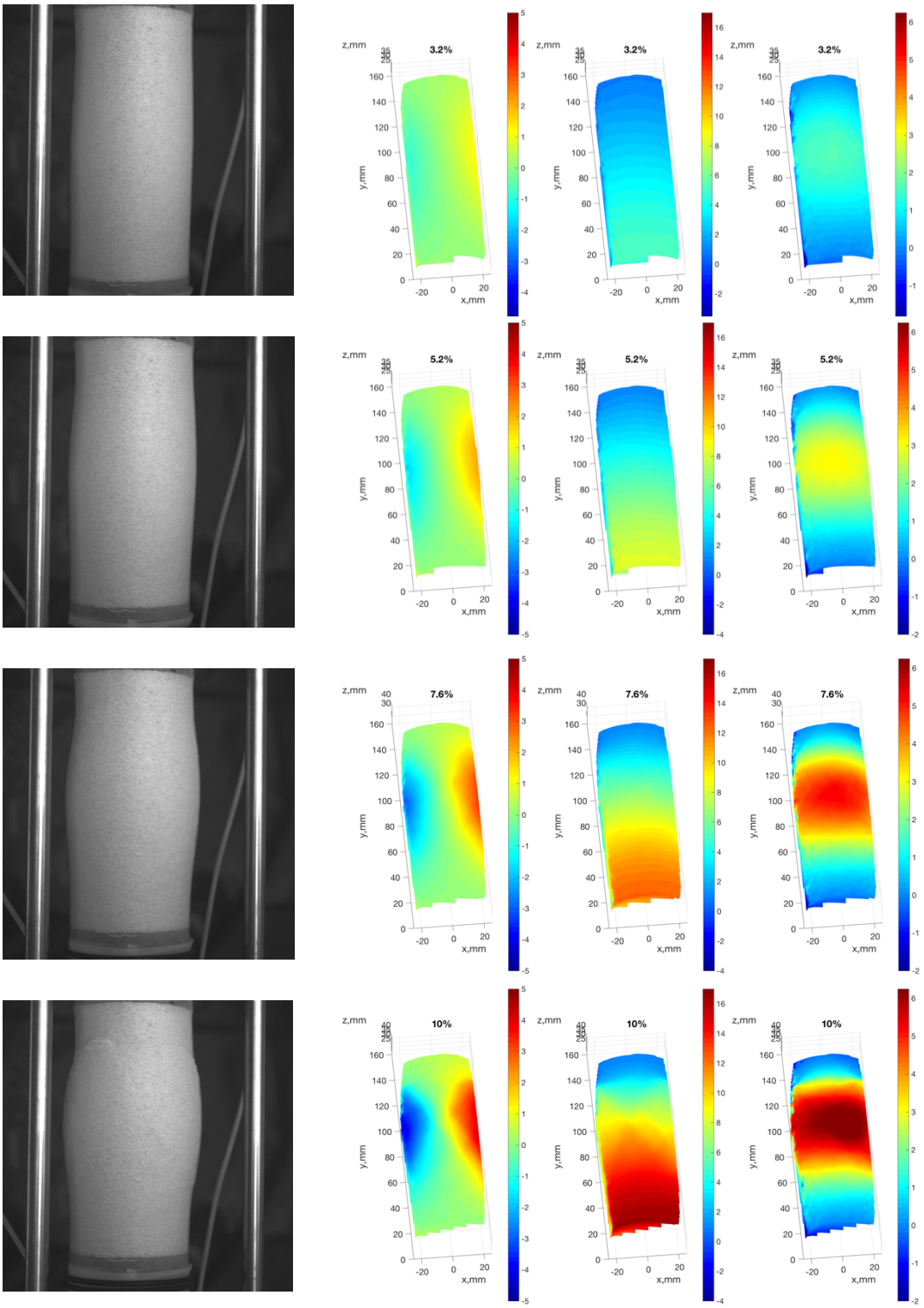


**Figure 4. 7 Test 121304c- Digital Images (Medina, 2006) and Displacement (cartesian) in Eulerian Description at 3. 2%, 5.2%, 7.2% and 10% axial strain. (Left) x- direction, (Middle) y- direction, (Right) z- direction**

Changes in the z-direction relates to bulging of sample out- of- the page. No changes in z- direction is observed along the top and bottom portion of the sample is observed. Bulging started to be significant slightly above the peak strain level and continue to develop and spread out throughout the height and width of the sample. The bulging area become more concentrated within the strain softening range. Within this range, the top and bottom of sample are acting as fixed end while loading proceeds at the lower section. As the sample reaches its densest state, the sample expands due restraint and loading from upper and lower portion of specimen.

The area of bulging observed in x- direction is similar to that of z-direction signifying sample is bulging outwards. Bulging area is observed to be off centered in the 121304b (loose), 121304c (60 kPa), and 121304d (20 kPa) samples. Bulging area is below mid- height of the sample for the loose specimen and the 20 kPa specimen. In contrast, the bulging area observed in the 60 kPa sample is located above mid- height of sample. Bulging observed for 40 kPa samples are located at mid- height of sample. Comparison of bulging zone observed in the z- direction is presented in figure 4.8.

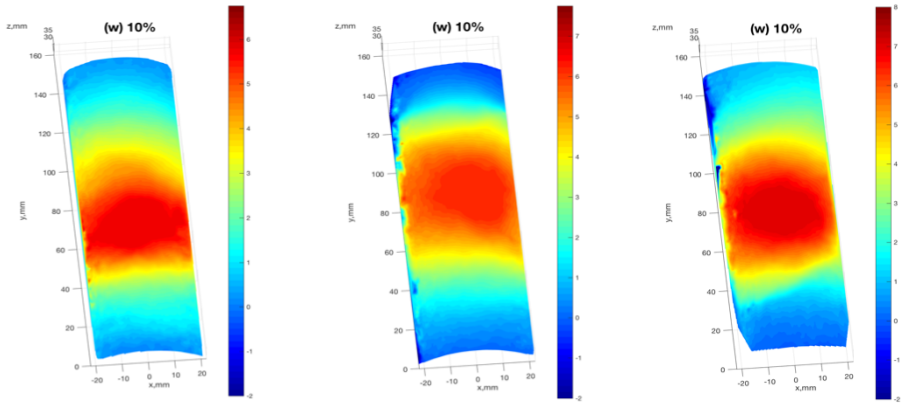


**Figure 4. 8 Off- centered bulging observed. Figure shown is at 10% axial strain level. From left to right: 121304b (loose), 121304c (60 kPa), 121304d (20kPa)**

### *4.2.2 Cylindrical Displacement Fields*

The displacement field in the cylindrical coordinate system is presented in figure 4.9 to 4.14. Positive radial displacement indicates that the sample is expanding (bulging) and vice versa negative radial displacement indicates the sample is compressing. Vertical bands of various magnitude of radial displacement developed at earlier strain (figure 4.15). Increase in radial displacement become more concentrated along the middle of the sample, due to restraint from the bottom and top platen. Highest displacement magnitude is observed at the middle of sample and decrease towards the top and bottom of specimen. The radial displacement is observed to increase clockwise about y- axis. Increase in radial displacement is initially observed to be minimal. Slightly before peak until end of softening, radial displacement is observed to increase more rapidly and slower within the constant volume strain range. The region where radial displacement occurs become localized in the middle while the top and bottom of specimen has minimal to zero radial displacement throughout the loading. Area of bulging stop to spread out at the end of softening. Similarity in bulging or out- of- page displacement characteristic is observed with that of displacement in z-direction.

The displacement observed in the tangential direction relates to the angular displacement in the x- z plane. Positive angular or tangential displacement indicates counter-clockwise displacement about the x-z plane or about the y- axis. Vertical bands of similar angular displacement magnitude are observed for all samples at strain level below 1 %, with exceptions to the 60 kPa specimen. The increase in angular displacement magnitude in all tests are observed to increase in clockwise direction. Above 1% strain,

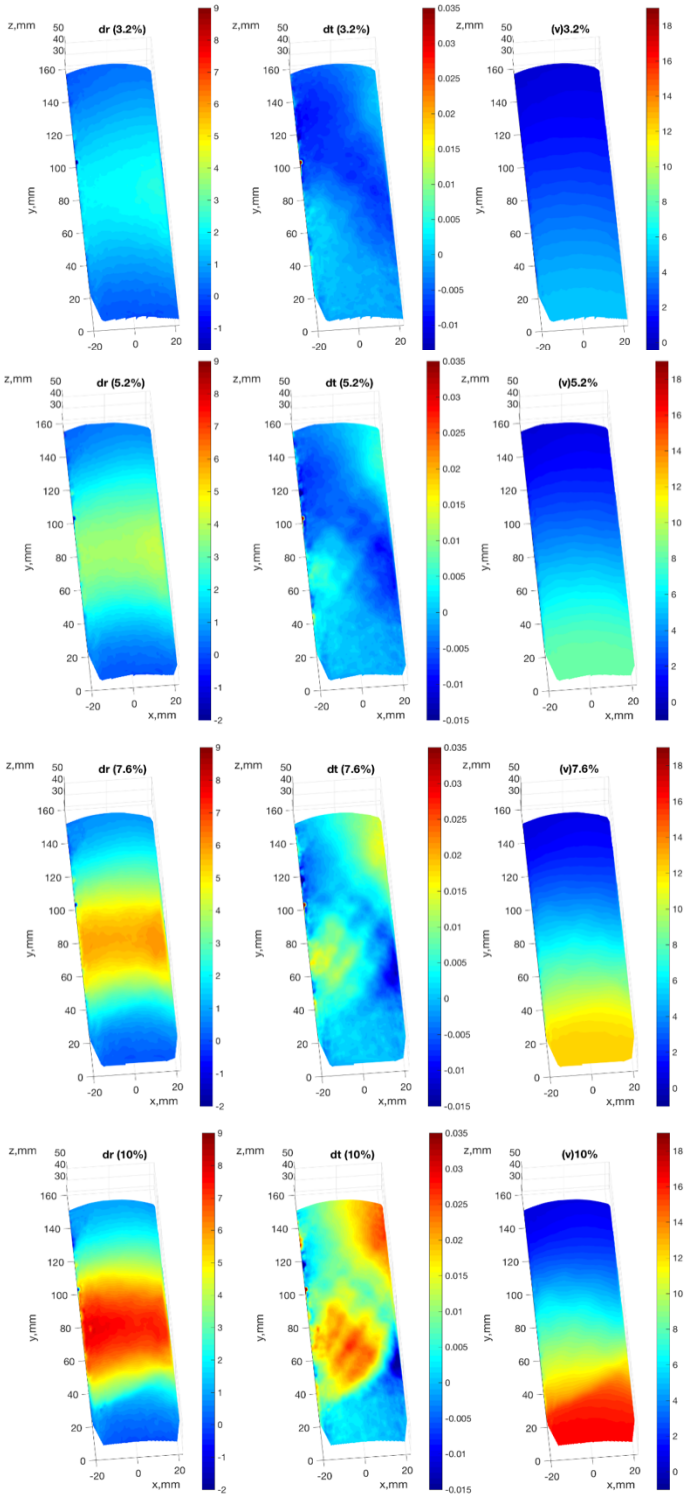


**Figure 4. 9 121304d (20kPa) Cylindrical Displacement in Lagrangian Description at 3.2%, 5.2%, 7.6%, and 10% axial strain. From left to right: radial displacement, tangential/ angular displacement, and vertical displacement**

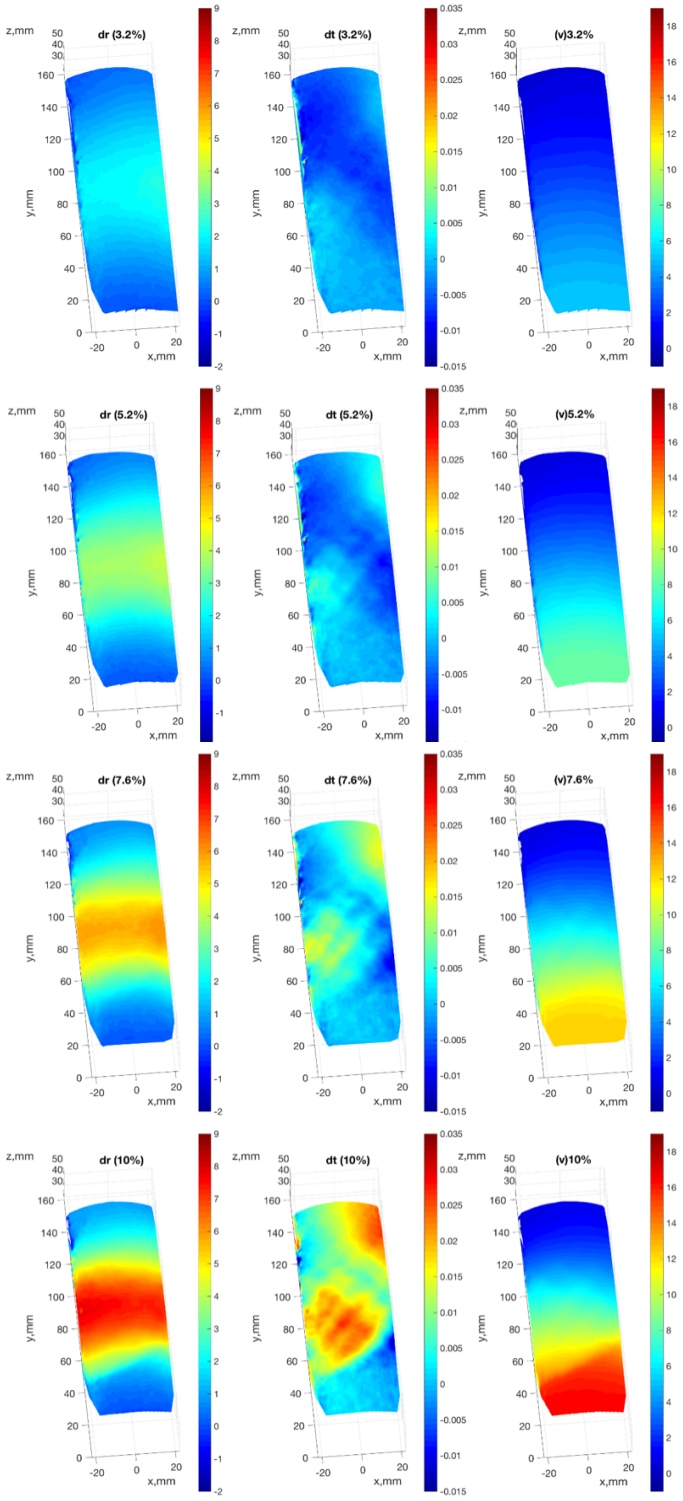


**Figure 4. 10 121304d (20kPa) Cylindrical Displacement in Eulerian Description at 3.2%, 5.2%, 7.6%, and 10% axial strain. From left to right: radial displacement, tangential/ angular displacement, and vertical displacement**

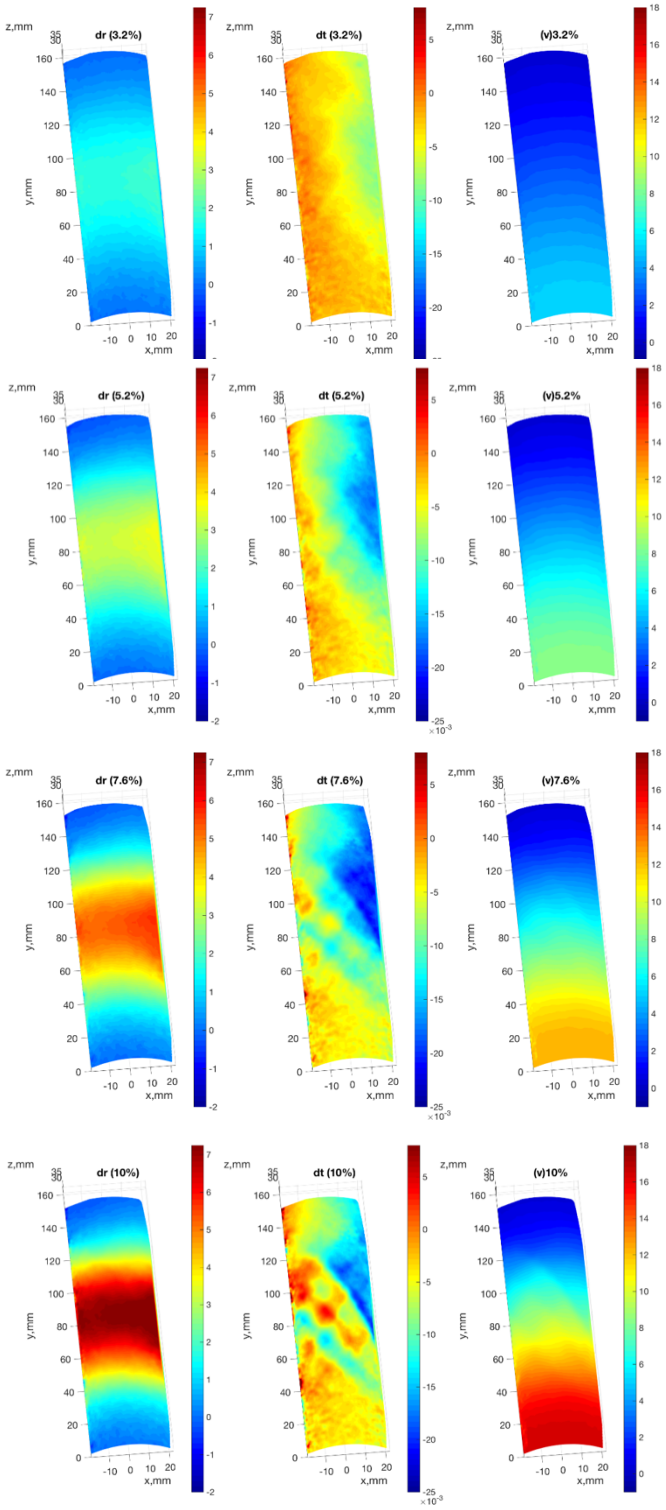


**Figure 4. 11 Test 121304a (40 kPa)- Displacement (cylindrical) in Lagrangian Description at 3. 2%, 5.2%, 7.2%, and 10% axial strain. (Left) radial, (Middle) tangential, and (Right) y-direction.**

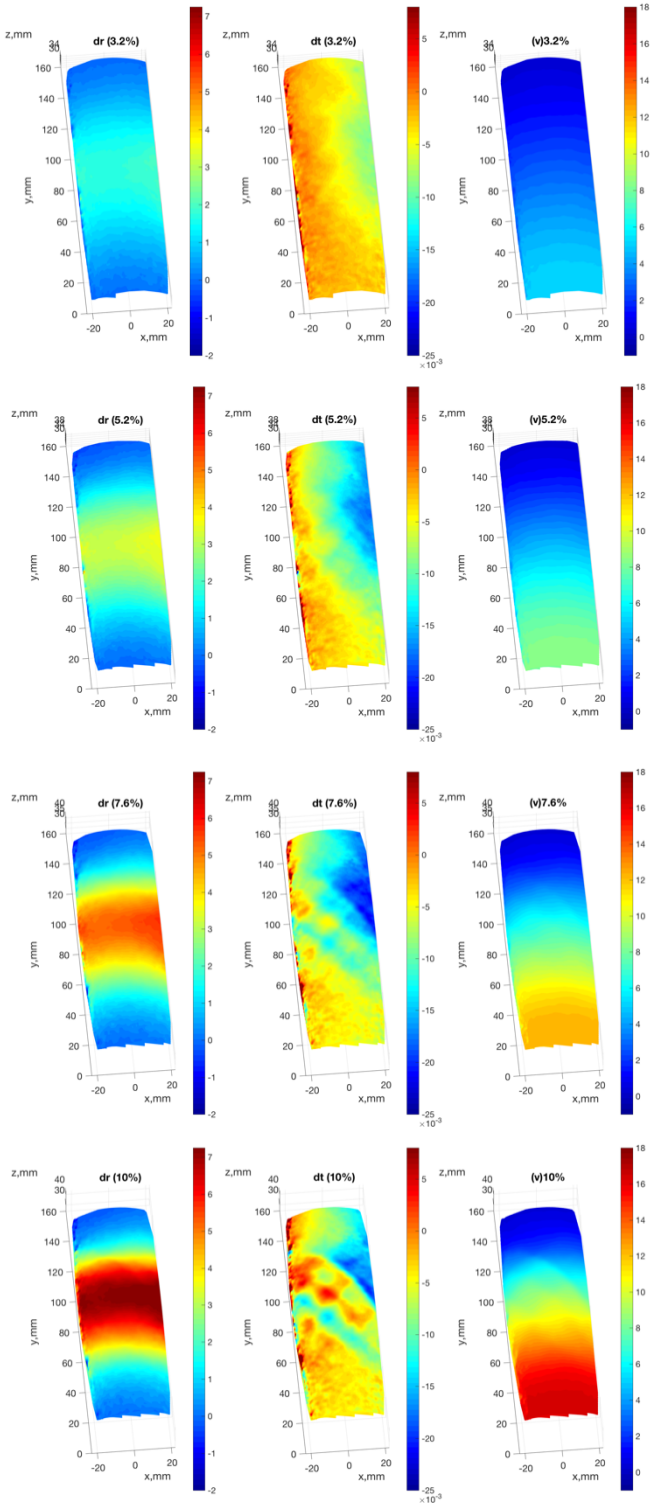


**Figure 4. 12 Test 121304a (40 kPa)- Displacement (cylindrical) in Eulerian Description at 3. 2%, 5.2%, 7.2%, and 10% axial strain. (Left) radial, (Middle) tangential, and (Right) y-direction.**

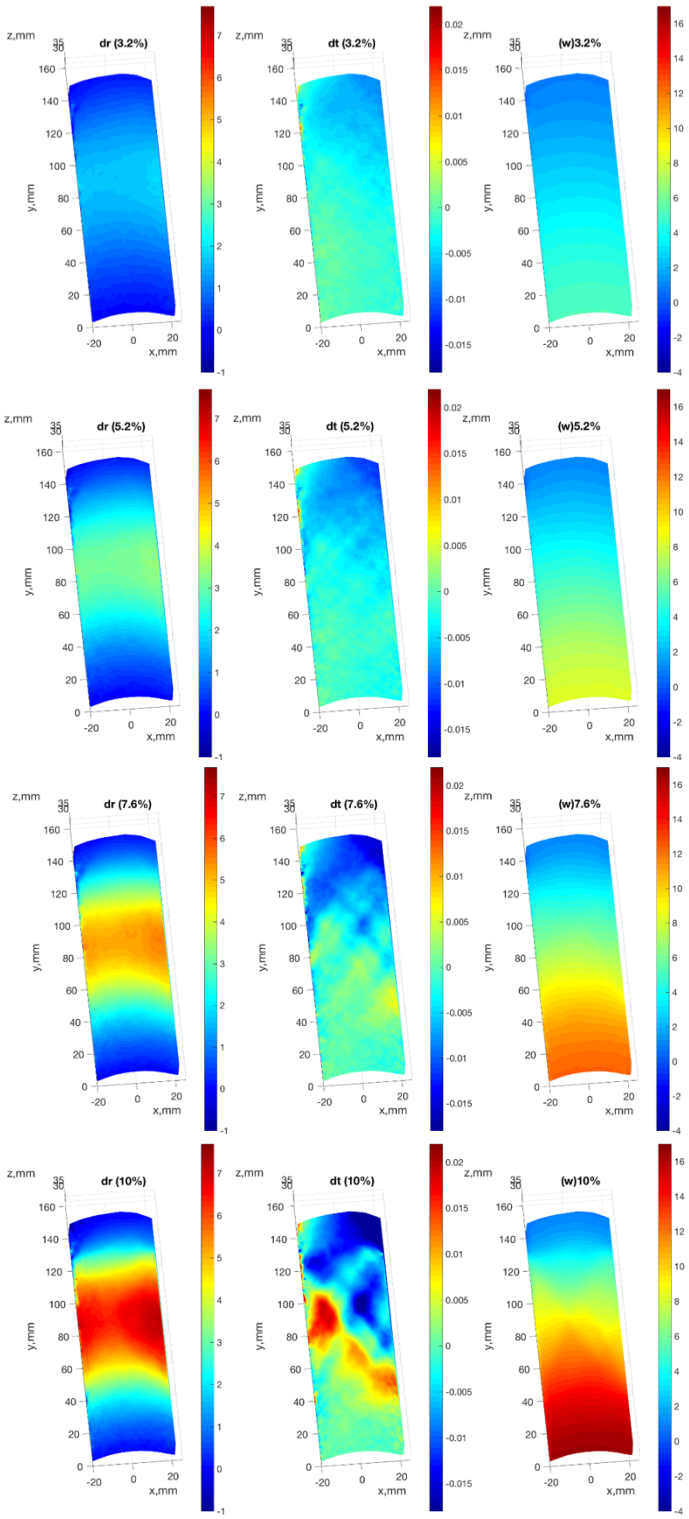


**Figure 4. 13 121304c (60 kPa) Cylindrical Displacement in Lagrangian Description at 3.2%, 5.2%, 7.6%, and 10% axial strain. From left to right: radial displacement, tangential/ angular displacement, and vertical displacement**

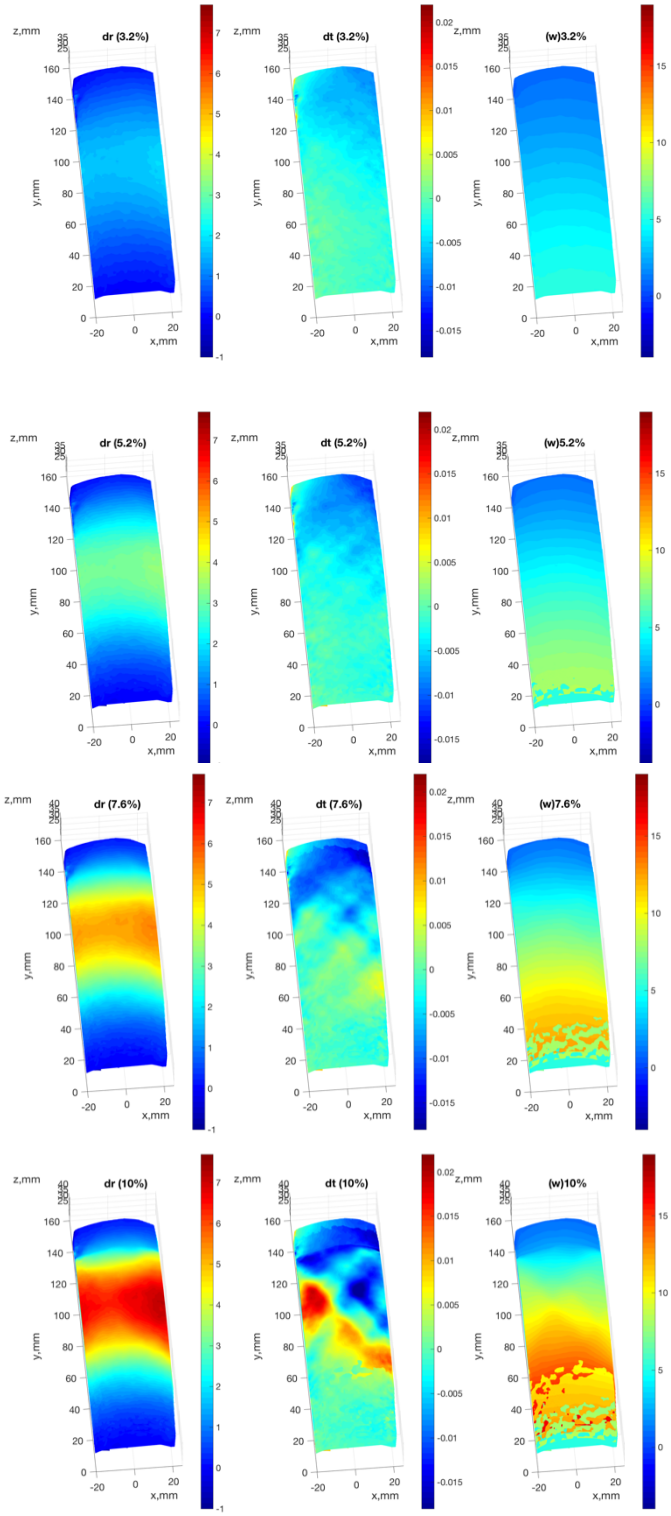


**Figure 4. 14 121304c (60 kPa) Cylindrical Displacement in Eulerian Description at 3.2%, 5.2%, 7.6%, and 10% axial strain. From left to right: radial displacement, tangential/ angular displacement, and vertical displacement**

higher magnitude of angular displacement is observed at the upper right of sample while zero magnitude angular displacement is observed to be minimal to none at the bottom of the sample. Contrasting magnitude between the upper right and bottom left of sample entrapped and induced diagonal localization across the middle of the sample. The localization is observed to form slightly after peak strength towards beginning of softening strain where low magnitude region is entrapped by higher magnitude angular displacement moving in clockwise direction. This localization would then develop into shear band during the softening (figure 4.16). Rotation within shear band observed is in contrast with the direction of angular displacement observe at the top and lower portion of the sample.

The characteristic of displacement in the x, z, and radial displacement shows the the expansion or compression observed. The y displacement shows how much the sample compresses along the height of the sample. Tangential or angular displacement defines how much rotation is observed along the x-z plane. Tangential displacement is found to shows signs of developing shear band. Similar displacement phenomenon is observed in the Lagrangian and Eulerian for all samples, with exceptions to test 101204a (40 kPa) in which tangential displacement is observed at the end of softening.

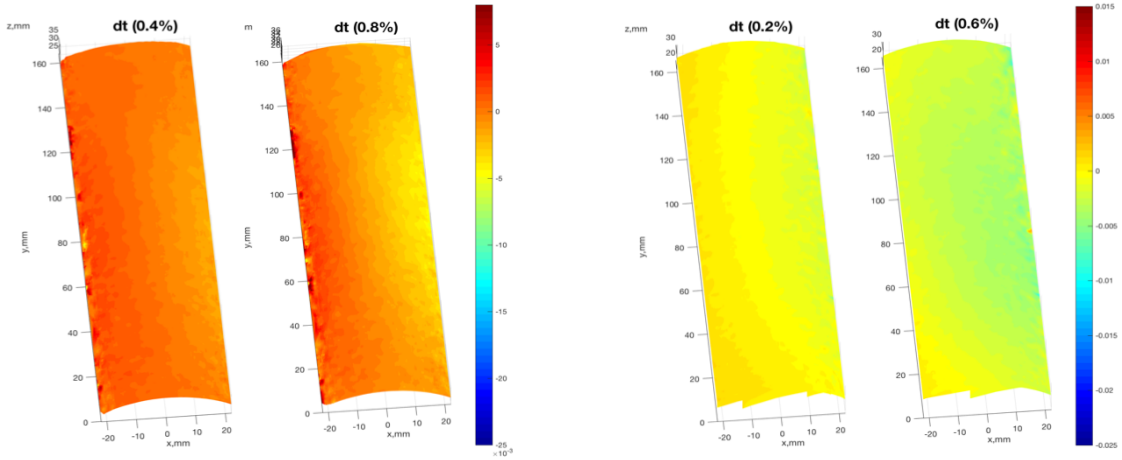


**Figure 4. 15 Vertical pattern in angular displacement. From left to right: 121304a tangential displacement at strain levels 0.4% and 0.8%, 101304a tangential displacement at 0.2% and 0.6% strain levels**

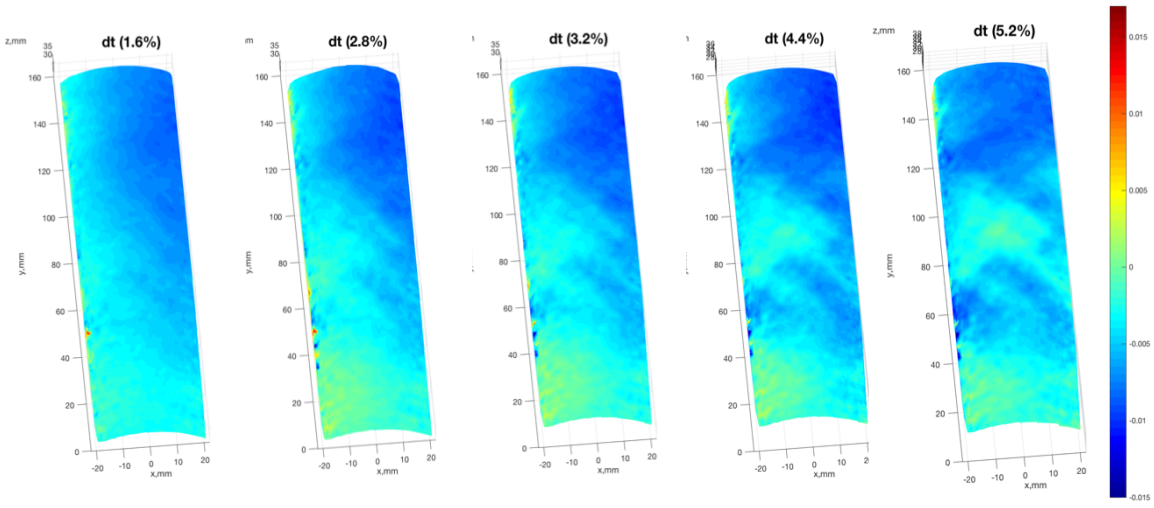


**Figure 4. 16 Test 121304b (Loose) - Formation of shear band due to contrasting tangential displacement initiated at lower left of specimen. Axial strain levels from left to right: 1.6%, 2.8%, 3.2%, 4.4%, and 5.2%.**

## 4.3 Divergence of Displacement Fields

The 2D material divergence about the x and y directions are shown in figure 4.17 through 4.19. Thresholds are set to correct noises observed. For all specimens, expansion band started to develop in the middle of the sample slightly before the peak strength. No pattern is observed initially. Little to no expansion is observed along the top and bottom part of sample. For the 60 kPa experiment, signs of localized high magnitude expansion band are observed to form after peak strength and continue to intensify within the softening region. Expansion bands are observed in all specimens. The expansion bands are observed to be more well- defined in the 60 kPa specimen compared to the 20 kPa and 40 kPa specimens. The length of expansion band observed in high confining sample is greater compared to the lower confinement specimens. More expansion bands are observed in the 20 kPa and 40 kPa specimens.

Compaction band is observed to develop starting the beginning of softening. Compaction band delaminate the expansion region observed at the middle with the rigid (zero to no expansion) in the upper and lower portion of sample. Varying location of compaction band is observed. In both 40 kPa specimens, compaction band is observed at the upper and lower boundary of expansion region. In the 60 kPa specimen, compression band is only observed at the upper part boundary of expansion region while it is located at the lower boundary of expansion region in the 20 kPa specimen. This observation is consistent with offset observed in the displacement field. No compaction band is observed in the loose specimen. At the end of softening, sudden increase in compaction band magnitude is observed consistent in all specimen.

Similar results are observed between Eulerian and Lagrangian description with exception to the loose specimen and localization observed in the Lagrangian description. Localization is observed more clearly in Lagrangian description compared to the Eulerian. The expansion van observed on the sides of specimen in Eulerian description indicates bulging observed in the x- direction.

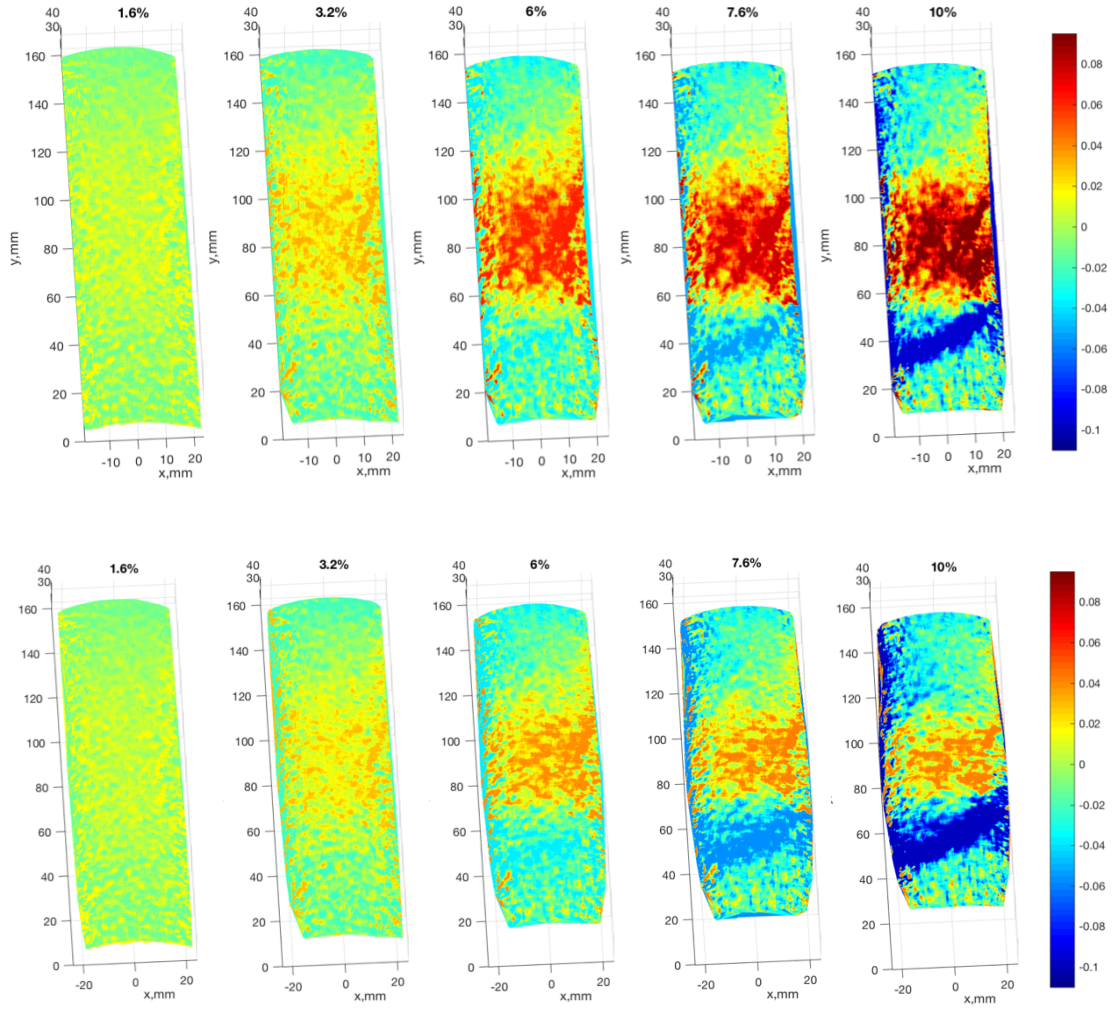


**Figure 4. 17 121304d (20 kPa) Divergence in Lagrangian Descriptions (Top) and Eulerian Description (Bottom) at 1.6%, 3.2%, 5.2%, 7.6%, and 10% axial strain**

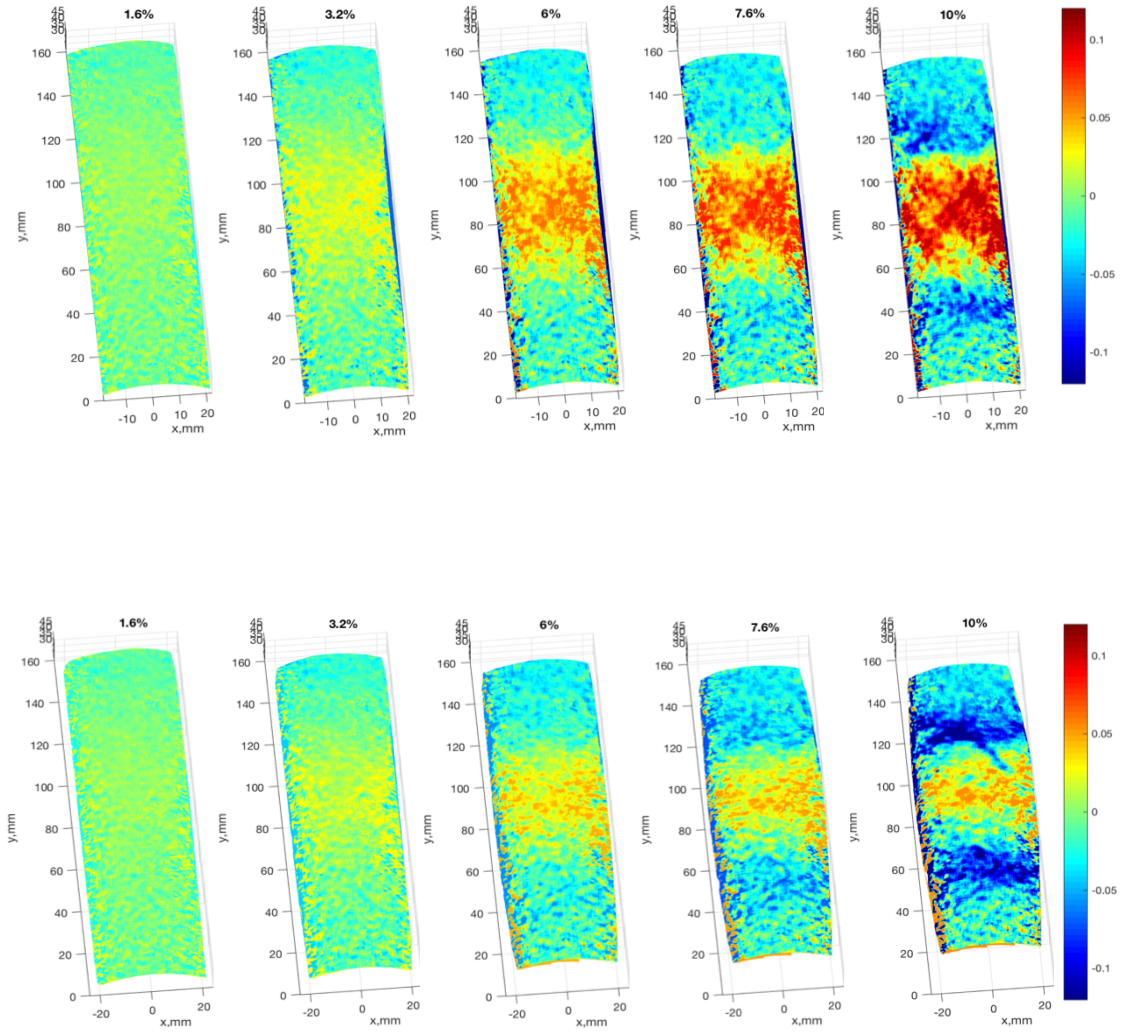


**Figure 4. 18 121304a (40 kPa) Divergence of displacement field at 1.6%, 3.2%, 5.2%, 7.2%, and 10% axial strain. (Top) Lagrangian Description. (Bottom) Eulerian Description**

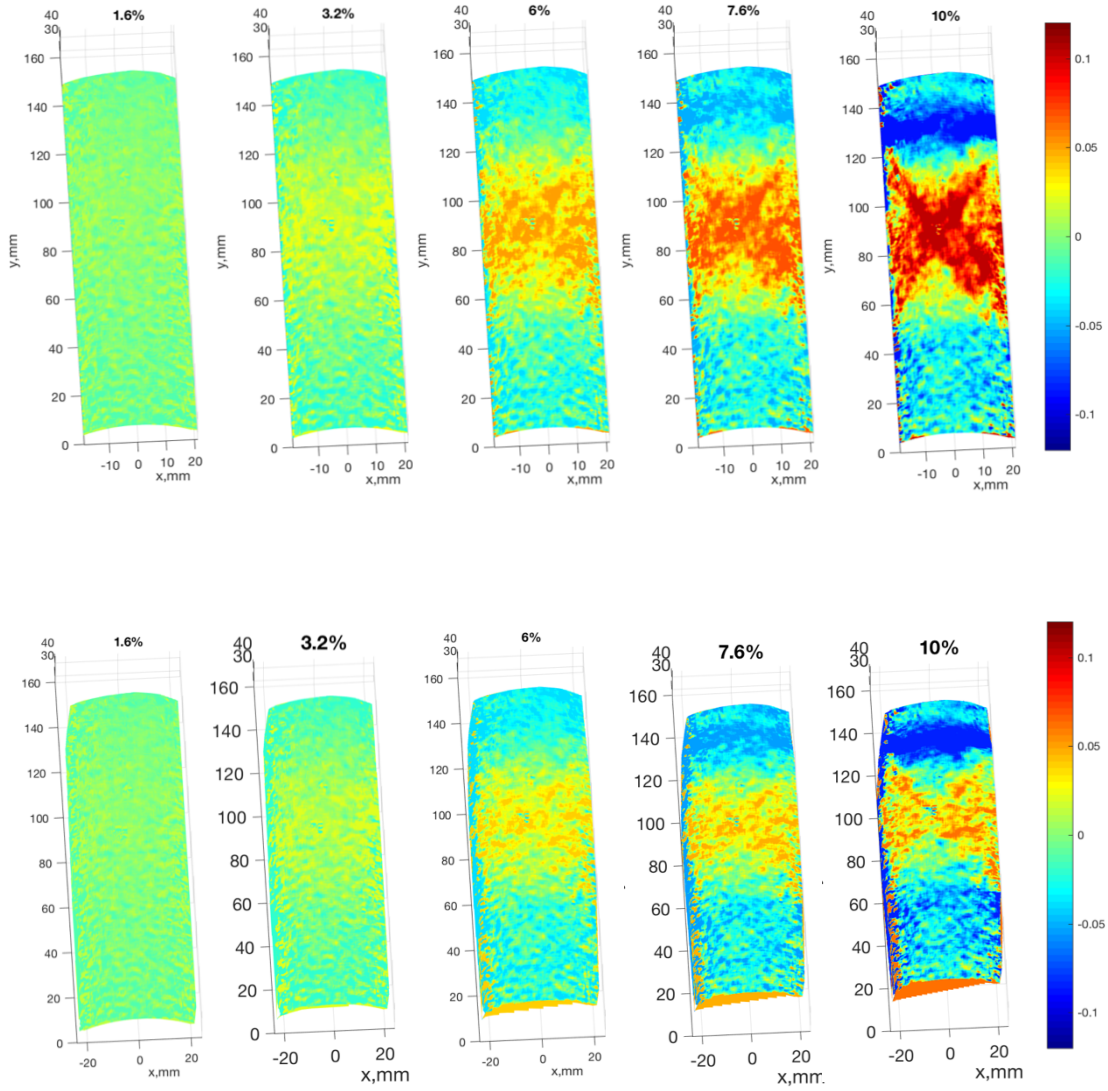


**Figure 4. 19 121304c (60 kPa) Divergence at 1.6%, 3.2%, 5.2%, 7.2%, and 10% in Lagrangian Description (Top) and Eulerian Description (Bottom)**

## 4.4 Curl of Displacement Fields

The curl of displacement field is analyzed about the x and y directions (figure 4.20 to 4.22). No patterns are initially observed at approximately below 1% axial strain. Localization in contrasting curl regions started to be observed above 1% axial strain. Rotations observed in the lower left and upper right of specimen is in counter- clockwise direction. Rotations around the lower right and upper left of specimen is observed to be zero initially. As loading progresses, increase in counter- clockwise magnitude induced the development of clockwise magnitude rotation at the initially zero magnitude region. This development is started to be observed starting from the beginning of strain softening or slightly after the peak strain.

Competing region of rotational bands is observed in the middle of sample. Rotation band started to occur slightly before peak strength and continue to localize in the strain softening region. Multiple clockwise and counter- clockwise bands (region with similar magnitude) is observed in the middle of the sample at end of softening. The following observation is consistent with what has been observed in both radial and tangential displacement.

More rotational bands are observed in loose and 20 kPa specimens (Figure 4.20). More resistance to rotation is observed in the 60 kPa specimen and less rotational band is observed. Signs of rotational bands are observed before the peak. The increase in magnitude observed in 60 kPa appears to progress slower than the remaining tests and localization appears more rapidly. Less bands are observed in the 60 kPa confinement

specimen in comparison to the 20 kPa and 40 kPa specimens. The following observation is consistent with what has been observed in the divergence of displacement. Curl obtained in both Lagrangian and Eulerian descriptions showed similar results. Thresholds are set to correct noises observed.

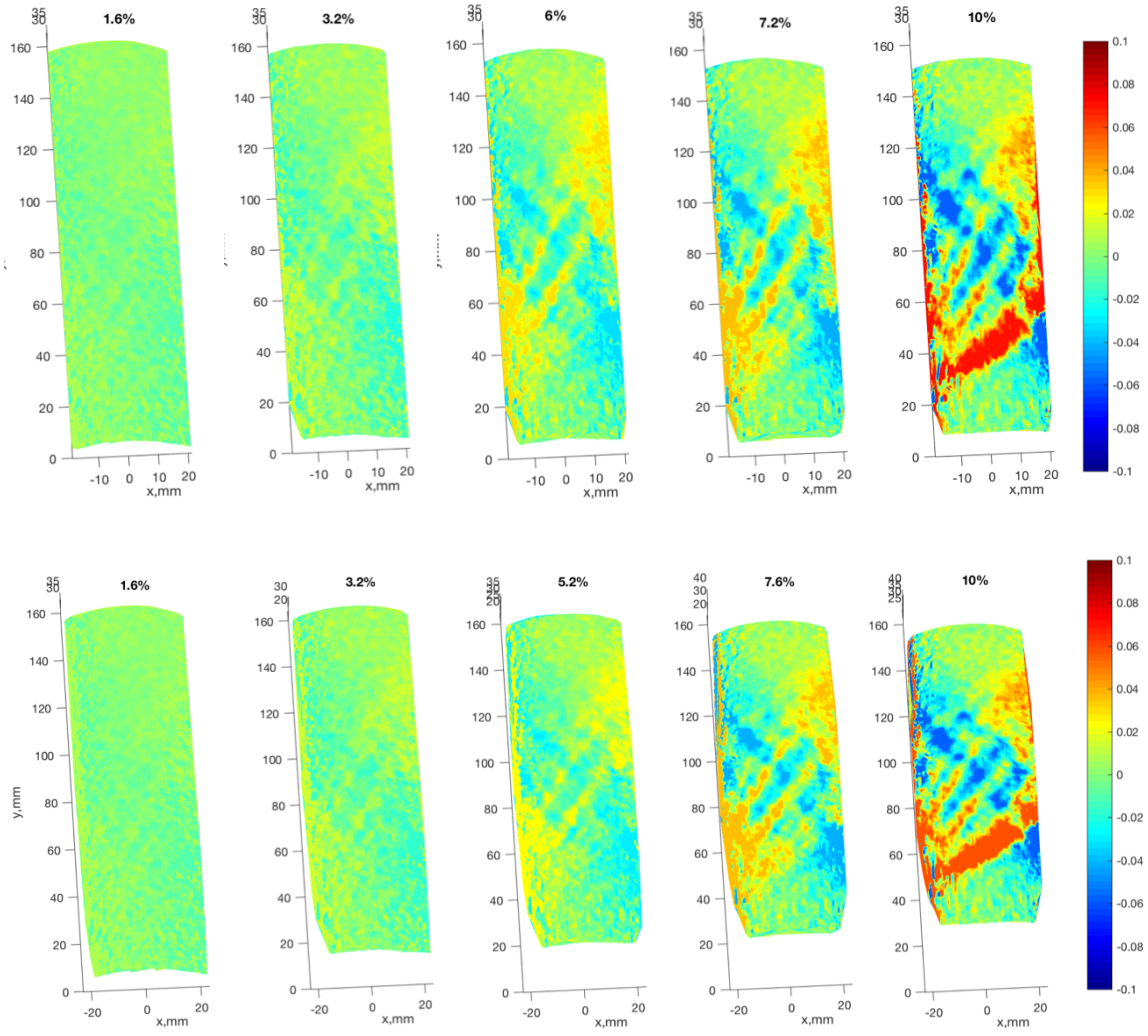


**Figure 4. 20 121304d (20 kPa) Curl in Lagrangian Description (TOP) and Eulerian Description (Bottom) at 1.6%, 3.2%, 6%, 7.2%, and 10% axial strain**

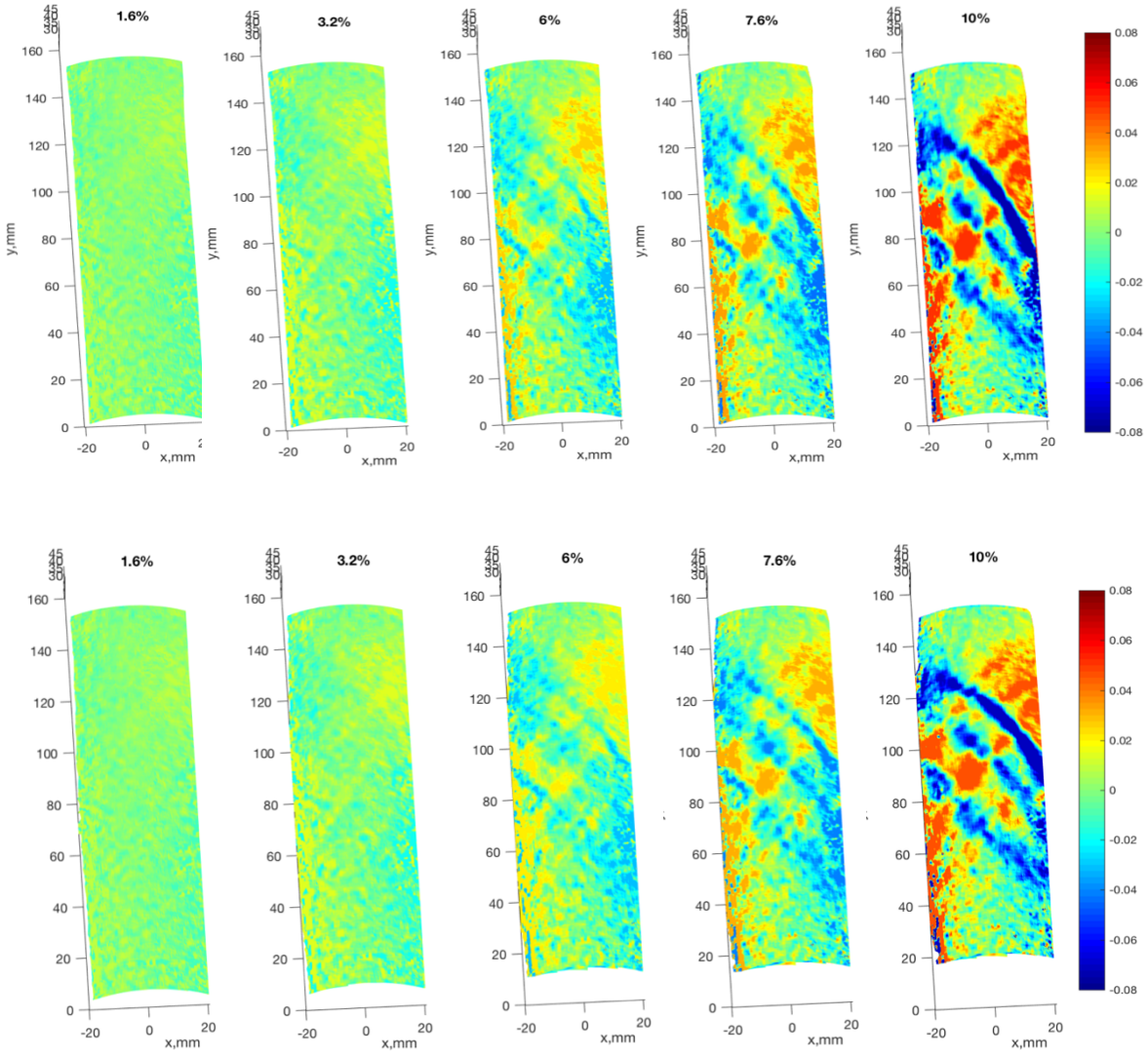


**Figure 4. 21 121304a (40 kPa)- Curl in Material Description (Top) and Eulerian Description (bottom) at 1.6%, 3.2%, 6%, 7.6%, and 10% axial strain**

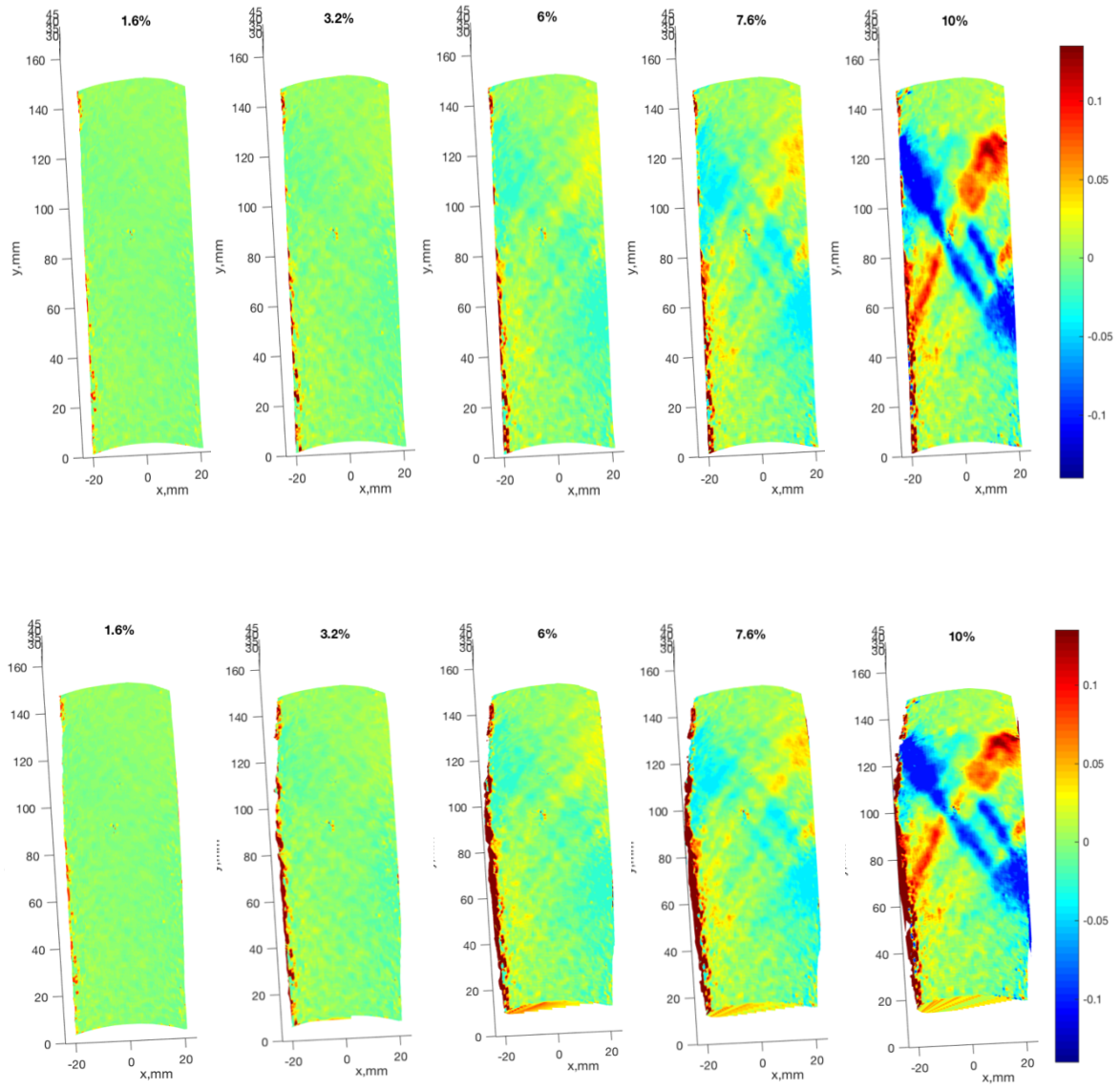


**Figure 4. 22 121304c (60 kPa) Curl in Lagrangian Description (Top) and Eulerian Description (Bottom) at 1.6%, 3.2%, 6%, 7.2%, and 10% axial strain**

## 4.5 Deformation Gradient

The deformation gradient for all tests are presented in figures 4.23 to 4.25. The deformation gradient presented is analyzed in Lagrangian description. Thus, the rate of translational and rotational changes observed represent the comparison between the deformed with that of the initial/ undeformed configuration. The deformation gradient is dimensionless quantity. Only translational component of deformation (diagonal terms) gradient will be discussed in this study. Thresholds are set to accommodate visualization of the gradient tensor components.

Changes observed in the x- direction initially is minimal to none. Positive magnitude of deformation gradient is observed in the middle part of sample approximately above earlier before peak strength. The magnitude of deformation gradient continues to increase along the middle of the sample. Initiation of localized expansion bands are observed before the peak strength. Expansion bands continue to increase in magnitude until the end of softening. Rapid increase in magnitude is observed at the end of softening. The pattern observed herein is similar to the pattern observed in Lagrangian divergence.

Immediately after loading, compressive band (negative magnitude) is observed in the y- direction deformation gradient. The band appear to extend vertically from the top of the sample and bend away into the horizontal direction slightly below the mid- height of sample. Regions with low to zero magnitude deformation gradient is observed outside the bands. Localized compression regions are observed to developed on an angle, connecting the horizontal compression region with the vertical compression region. At higher magnitude, the pattern observed is similar to corresponding curl and expansion

band pattern observed. The deformation gradient observed about z- direction appear to be scattered and slight localization is observed in the middle of the sample.

Similar patterns are observed throughout the test. The 60 kPa test shows much more homogeneous gradient field and more localized bands while scattering in pattern is observed more in the loose, 20 kPa, and 40 kPa specimens.

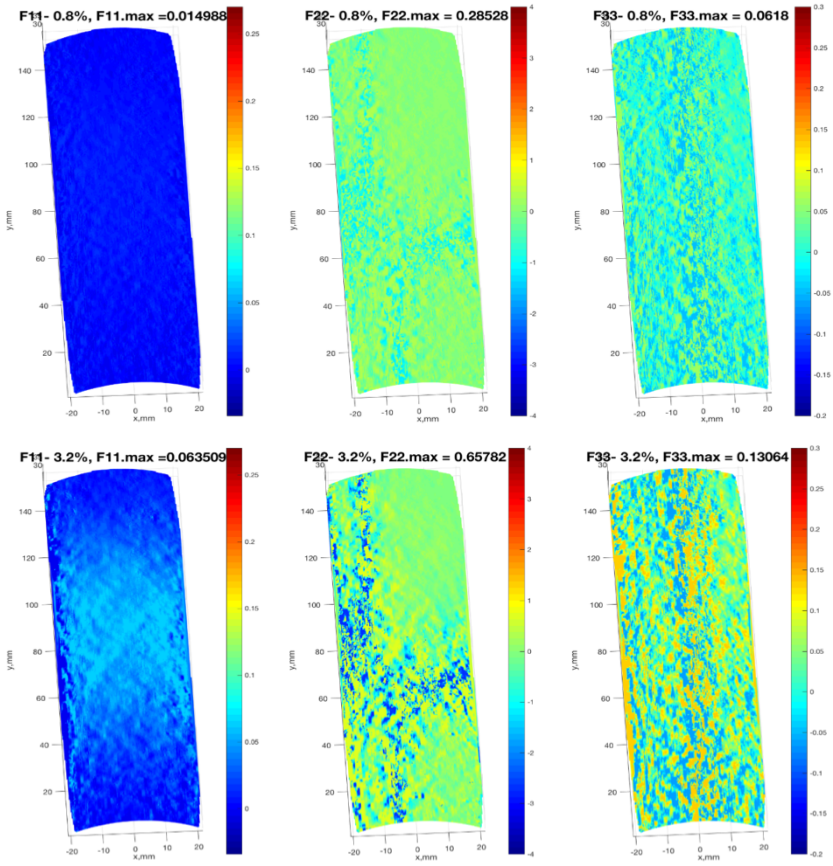


**Figure 4. 23 121304a (40 kPa)-Deformation gradient at 0.8% and 3.2% axial strain. From left to right: x, y , and z- direction deformation gradient.**

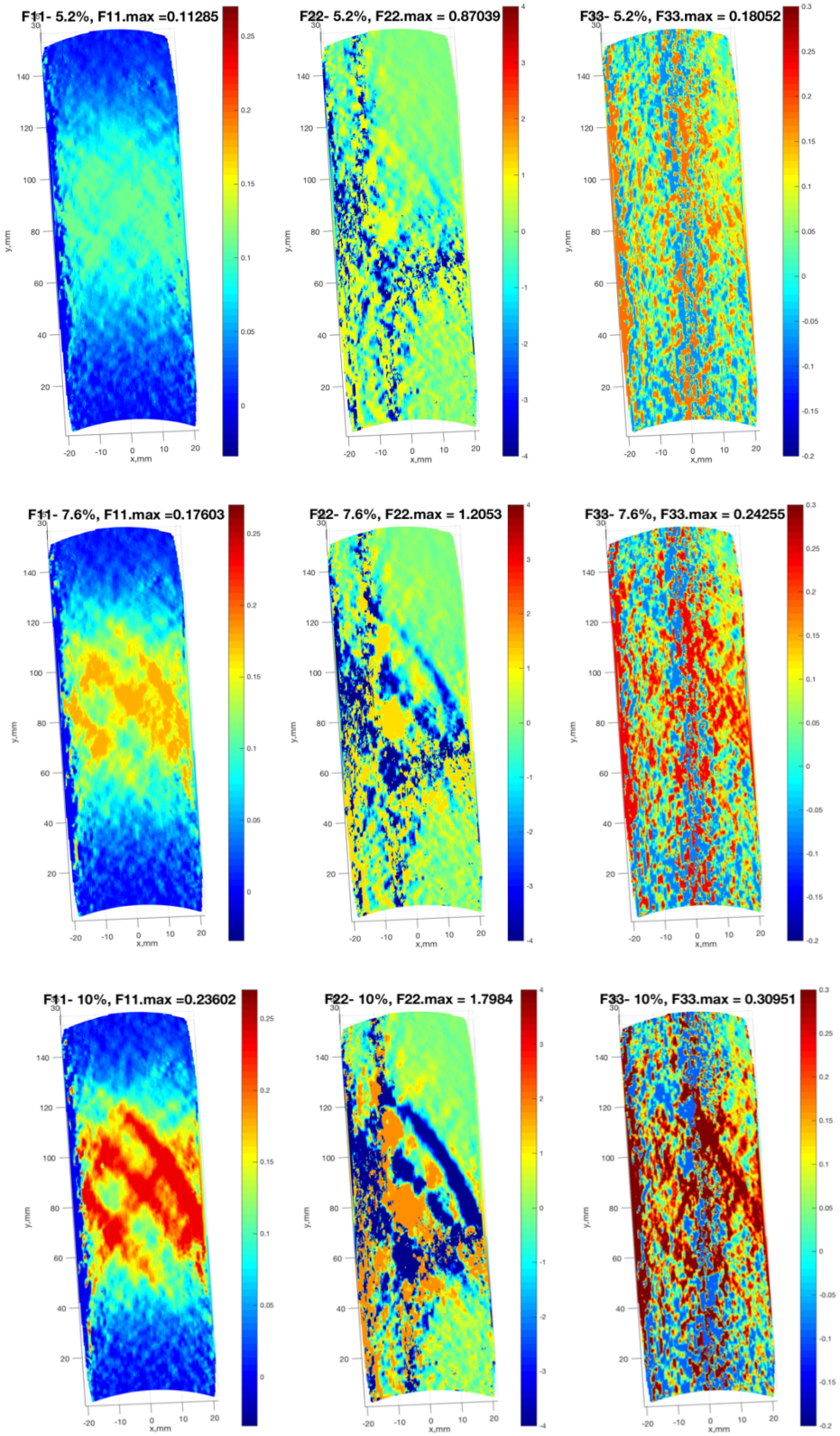


**Figure 4. 23 (continued) 121304a (40 kPa)- Deformation gradient at 7.6% and 10 % axial strain. From left to right: x, y , and z- direction deformation gradient.**

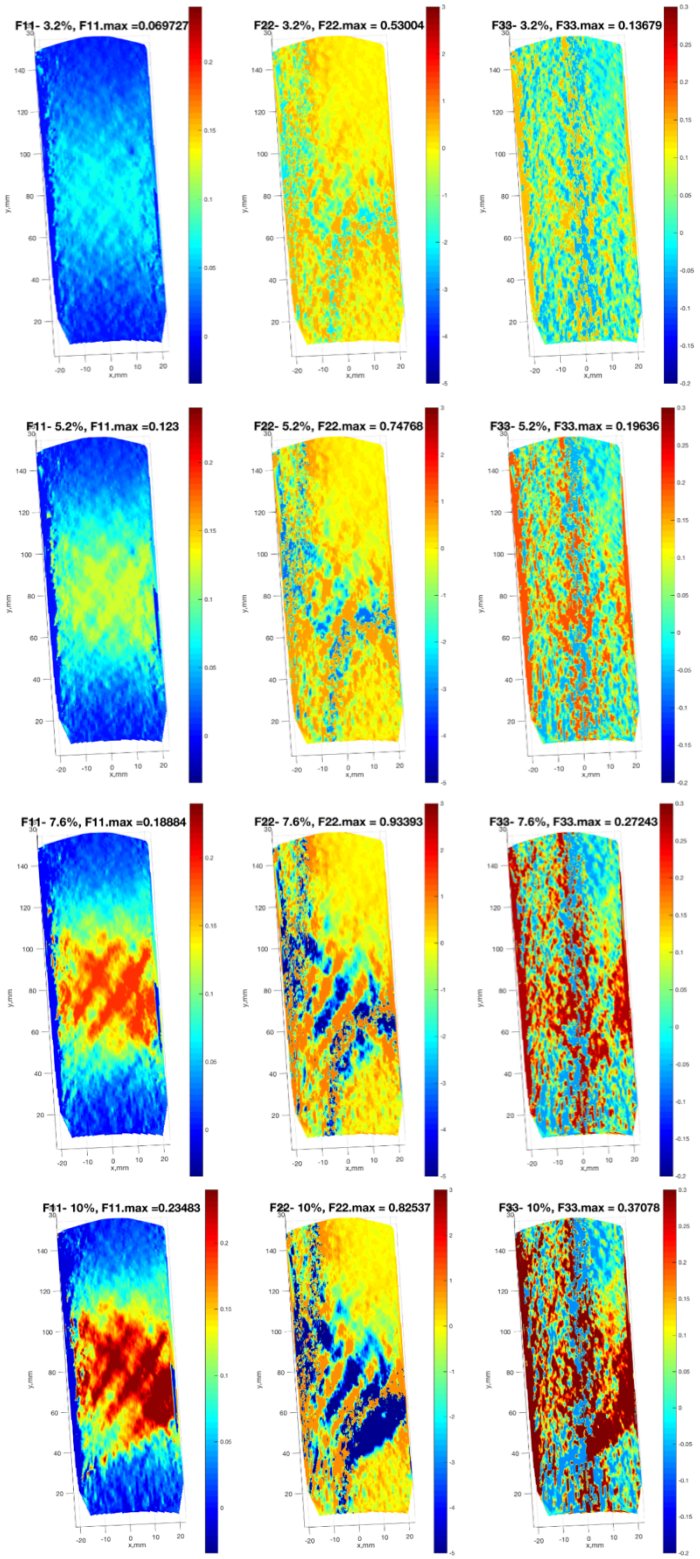


**Figure 4. 24 121304d (20 kPa)-Deformation gradient at 3.2%, 5.2%, 7.6 % and 10% axial strain. From left to right: x, y , and z- direction deformation gradient.**

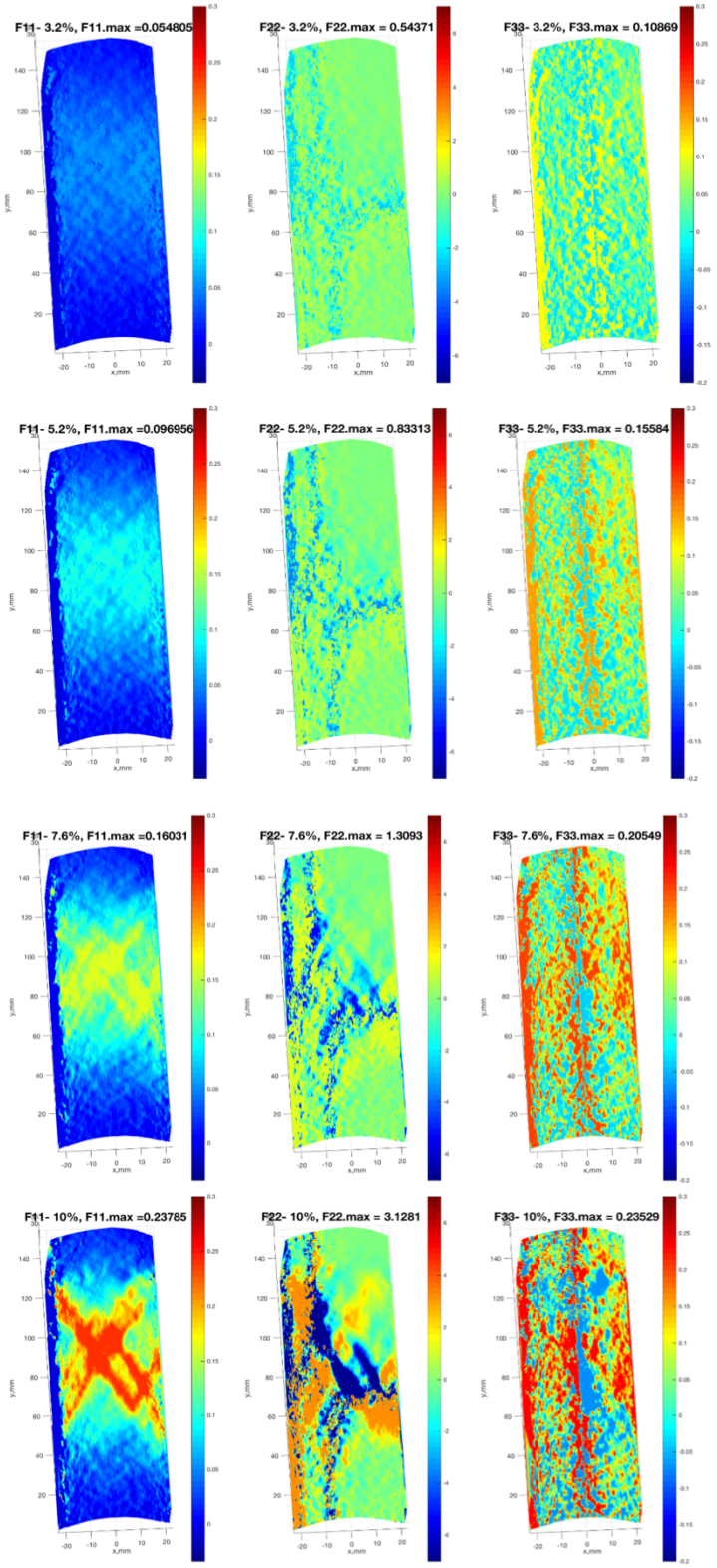


**Figure 4. 25 121304c (60 kPa)-Deformation gradient at 3.2%, 5.2%, 7.6 % and 10% axial strain. From left to right: x, y , and z- direction deformation gradient.**

# 5. SUMMARY AND CONCLUSION

A kinematic analysis on deforming sand compression specimens was performed on post- processed and calibrated 3D-DIC displacement fields. The concepts of divergence, curl, and the gradient were implemented to understand the development of localization effects, including shear and compaction bands. Both Lagrangian and Eulerian approach were attempted in the analysis. In addition, the cylindrical coordinate system was also considered in the analysis.

Changes in the magnitude of displacement were observed in both cylindrical and Cartesian coordinate systems. The development of shear bands was not clearly observed in the Cartesian system, except for the y- direction. Only effects of bulging and compression can be traced in the Cartesian system. Bulging and localization effects observed in the shear band are shown clearly in the tangential and vertical component displacement fields.

The results of the divergence of displacement fields shows the development of shear and/or compaction bands starting the beginning of strain softening. Localized rotational bands from the curl of the displacement field were observed within the localized shear/ compaction bands. Observation on the translational rate of change in the x- direction (gradient) was similar to the expansion/ compression characteristic observed in the divergence of displacement fields. The translational rate of change in the y- direction showed a similar pattern with observed expansion bands and curl localizations.

Effects of varying confining pressure on deformation had also been observed. Similarity was observed in the development of displacement fields, divergence, curl, and the gradient of displacement fields. Early indications of localization were observed starting beginning of strain softening or slightly after peak strength. The bulging observed through the radial, x, and y direction is located off- centered for the 20 kPa and 60 kPa specimens. Localization effects observed in the 60 kPa sample appeared to develop rapidly at higher strain level. The localization effects observed in the 20 kPa and 40 kPa samples were observed to develop progressively. Multiple shear bands were observed in the 20 kPa and the 40 kPa specimens while less shear bands were observed in the 60 kPa specimen. The shear bands in 60 kPa specimen was observed to be more well- defined compared to the other specimens. Single compaction (compression) band was observed in the 20 kPa and 60 kPa specimens while two compaction bands were observed for 40 kPa specimen. Compaction band observed in 20 kPa specimen at lower part of bulging region while it was observed above the bulging region for the 60 kPa specimen and above and below bulging region for the 40 kPa specimen. Based on the gradient of displacement observed, a narrower localized band is observed for the 60 kPa specimen in comparison with the 20 kPa and the 40 kPa specimen. Less scattering was observed in the gradient field with decrease in confinement.

Early indications of localization effects had been observed through divergence, curl, and gradient of displacement fields. The development of localization effects observed through the utilization of continuum kinematics operators of 3D- displacement fields was identified as early as the beginning of strain softening or slightly after peak strength. The

development of localization observed visually by human eye was identified at the end of strain softening towards the beginning of the critical state. The effect of confining pressure was seen in the duration of localization development (rapid or slow progression), and location of observed compaction bands or area of bulging observed.

The analysis of divergence and curl of displacement fields were done in 2D while 3D analysis is performed on the gradient of displacement fields. Further study with more experimental data needs to be performed to validate findings observed in this study. Future study should consider the third dimension provided by the 3D- DIC technique into the analysis. In addition, future study may also incorporate the cylindrical coordinate system in executing the kinematics analysis, which was not attempted in this study.

# REFERENCES


Abedi, Sara. (2012). Meso-scale kinematics in shear bands and impact of material heterogeneity on shear band development in sand. PhD Dissertation, University of Southern California, Los Angeles, CA.

Alikarami, R., Andò, E., Gkiousas-Kapnisis, M., Torabi, A., & Viggiani, G. (2014). Strain localisation and grain breakage in sand under shearing at high mean stress: insights from in situ X-ray tomography. *Acta Geotechnica*, *10*(1), 15–30. https://doi.org/10.1007/s11440-014-0364-6

Alshibli, K., Sture, S., Costes, N. C., & Frank, M. L. (2000). Assessment of localized deformations in sand using X-ray computed tomography. *ASTM Geotechnical Testing Journal*. Retrieved from http://cat.inist.fr/?aModele=afficheN&cpsidt=1499224%5Cnpapers3://publication/uuid/C7DE2243-8C5D-4698-A0E5-589E288DD1FD

Alshibli, K. A., & El-Saidany, H. A. (2001). Quantifying Void Ratio in Granular Materials Using Voronoi Tessellation. *Journal of Computing in Civil Engineering*, *15*(3), 232–238. https://doi.org/10.1061/(ASCE)0887-3801(2001)15:3(232)

Andò, E., Hall, S. A., Viggiani, G., Desrues, J., & Bésuelle, P. (2012). Grain-scale experimental investigation of localised deformation in sand: A discrete particle tracking approach. *Acta Geotechnica*, *7*(1), 1–13. https://doi.org/10.1007/s11440-011-0151-6

Banks, H. T., Hu, S., & Kenz, Z. R. (2011). A brief review of elasticity and viscoelasticity for solids. *Advances in Applied Mathematics and Mechanics*. https://doi.org/10.4208/aamm.10-m1030

Besuelle, P., & Rudnicki, J. W. (2003). Chapter 5 Localization: Shear bands and compaction bands. *International Geophysics*, *89*(C), 219–321. https://doi.org/10.1016/S0074-6142(03)80021-9

Belytschko, T., Liu, W., & Moran, B. (2000). *Nonlinear finite elements for continua and structures. 2000*. *Chichester, New York, John Wiley* (Vol. 16). https://doi.org/10.1016/S0065-230X(09)04001-9

Boldyrev, G. G. and Muyzemnek, A. J., "The Modeling of Deformation Process in Soils With Use of Ansys and Ls-Dyna Programs" (2008). International Conference on Case Histories in Geotechnical Engineering. 37. http://scholarsmine.mst.edu/icchge/6icchge/session_01/37

Borja, R. I., & Alarcón, E. (1995). A mathematical framework for finite strain elastoplastic consolidation Part 1: Balance laws, variational formulation, and linearization. *Computer Methods in Applied Mechanics and Engineering*, *122*(1–2), 145–171. https://doi.org/10.1016/0045-7825(94)00720-8

Borja, R. I., Song, X., Rechenmacher, A. L., Abedi, S., & Wu, W. (2013). Shear band in sand with spatially varying density. *Journal of the Mechanics and Physics of Solids*, *61*(1), 219–234. https://doi.org/10.1016/j.jmps.2012.07.008

Butterfield, R., Harkness, R. M., & Andrews, K. Z. (1970). A Stero-Photogrammetric Method for Measuring Displacement Fields. *Géotechnique*, *20*(3), 308–314. https://doi.org/10.1680/geot.1970.20.3.308

Cil, M. B., & Alshibli, K. A. (2014). 3D analysis of kinematic behavior of granular materials in triaxial testing using DEM with flexible membrane boundary. *Acta Geotechnica*, *9*(2), 287–298. https://doi.org/10.1007/s11440-013-0273-0

Cil, M. B., Alshibli, K. A., Desrues, J., Alshibli, K. A., & El-Saidany, H. A. (2001). 3D analysis of kinematic behavior of granular materials in triaxial testing using DEM with flexible membrane boundary. *Acta Geotechnica*, *9*(2), 287–298. https://doi.org/10.1061/(ASCE)0887-3801(2001)15:3(232)

Clayton, J. (2011). On anholonomic deformation, geometry, and differentiation. *Mathematics and Mechanics of Solids*, *17*(7), 702–735. https://doi.org/10.1177/1081286511429887

Daehne, A., & Corsini, A. (2013). Kinematics of active earthflows revealed by digital image correlation and DEM subtraction techniques applied to multi-temporal LiDAR data. *Earth Surface Processes and Landforms*, *38*(6), 640–654. https://doi.org/10.1002/esp.3351

Desrues, J. (2004). Tracking strain localization in geomaterials using computerized tomography. *Xray CT for Geomaterials: Soils, Concrete, Rocks International Workshop on Xray CT for Geomaterials, Kumamoto, Japan*, 15–41. Retrieved from http://books.google.com/books?hl=en&lr=&id=v7hrx6FjwL8C&oi=fnd&pg=PA15&dq=Tracking+Strain+Localization+In+Geomaterials+Using+Computerized+Tomography&ots=cobGuP633_&sig=16ZHE3kshOafyQXL1VPH8C2fhro

Desrues, J., & Viggiani, G. (2004). Strain localization in sand: An overview of the experimental results obtained in Grenoble using stereophotogrammetry. *International Journal for Numerical and Analytical Methods in Geomechanics*, *28*(4), 279–321. https://doi.org/10.1002/nag.338

Drescher, A., & de Josselin de Jong, G. (1972). Photoelastic verification of a mechanical model for the flow of a granular material. *Journal of the Mechanics and Physics of Solids*, *20*(5), 337–340. https://doi.org/10.1016/0022-5096(72)90029-4

Fennema, C. L., & Thompson, W. B. (1979). Velocity determination in scenes containing several moving objects. *Computer Graphics and Image Processing*, *9*(4), 301–315. https://doi.org/10.1016/0146-664X(79)90097-2

Hall, S. A., Bornert, M., Desrues, J., Pannier, Y., Lenoir, N., Viggiani, G., & Bésuelle, P. (2010). Discrete and continuum analysis of localised deformation in sand using X-ray μCT and volumetric digital image correlation. *Géotechnique*, *60*(5), 315–322. https://doi.org/10.1680/geot.2010.60.5.315

Hall, S. A., Desrues, J., Viggiani, G., Besuelle, P., & Ando, E. (2012). Experimental characterisation of (localised) deformation phenomena in granular geomaterials from sample down to inter-and intra-grain scales. In *Procedia IUTAM* (Vol. 4, pp. 54–65). https://doi.org/10.1016/j.piutam.2012.05.007

Hasan, A., & Alshibli, K. (2010). Experimental assessment of 3D particle-to-particle interaction within sheared sand using synchrotron microtomography. Geotechnique, 60(5), 369-379. doi:10.1680/geot.2010.60.5.369

Higo, Y., Oka, F., Sato, T., Matsushima, Y., & Kimoto, S. (2013). Investigation of localized deformation in partially saturated sand under triaxial compression using microfocus X-ray CT with digital image correlation. *Soils and Foundations*, *53*(2), 181–198. https://doi.org/10.1016/j.sandf.2013.02.001

Ibrahimbegovic, A. (2009). Nonlinear solid mechanics. *Solid Mechanics and Its Applications*, *160*, 1–594. https://doi.org/10.1007/978-90-481-2331-5_1

Iwashita, K., & Oda, M. (2000). Micro-deformation mechanism of shear banding process based on modified distinct element method. Powder Technology, 109(1-3), 192-205.

Lai, A. C. K., & Chen, F. Z. (2007). Comparison of a new Eulerian model with a modified Lagrangian approach for particle distribution and deposition indoors. *Atmospheric Environment*, *41*(25), 5249–5256. https://doi.org/10.1016/j.atmosenv.2006.05.088

Liu, J. Y., Liu, M. L., & Zhu, Z. D. (2012). Sand Deformation around an Uplift Plate Anchor. *Journal of Geotechnical and Geoenvironmental Engineering*, *138*(6), 728–737. https://doi.org/Doi 10.1061/(Asce)Gt.1943-5606.0000633

Liyanapathirana, D. S. (2009). Arbitrary Lagrangian Eulerian based finite element analysis of cone penetration in soft clay. *Computers and Geotechnics*, *36*(5), 851–860. https://doi.org/10.1016/j.compgeo.2009.01.006

Marimon Giovannetti, L., Banks, J., Turnock, S. R., & Boyd, S. W. (2017). Uncertainty assessment of coupled Digital Image Correlation and Particle Image Velocimetry for fluid-structure interaction wind tunnel experiments. *Journal of Fluids and Structures*, *68*, 125–140. https://doi.org/10.1016/j.jfluidstructs.2016.09.002

Mathisen, K.M. (2012). Solution Methods for Nonlinear Finite Element Analysis (NFEA) [PowerPoint slides]. Retrieved Norwegian University of Science and Technology sintef site.

Medina-Cetina , Z. (2006). Probabilistic calibration of a soil model. PhD Dissertation, The Johns Hopkins University, Baltimore, MD.

Medina-Cetina, Z. (2016). *Geomechanics* [PowerPoint slides]. Retrieved from Texas A&M University CVEN 651 e-campus site.

Mooney, M. A., Finno, R. J., & Viggiani, M. G. (1998). A unique critical state for sand? *Journal of Geotechnical and Geoenvironmental Engineering*, *124*(11), 1100–1108. https://doi.org/10.1061/(ASCE)1090-0241(1998)124:11(1100)

Nazem, M., Sheng, D., Carter, J. P., & Sloan, S. W. (2008). Arbitrary Lagrangian-Eulerian method for large-strain consolidation problems. *International Journal for Numerical and Analytical Methods in Geomechanics*, *32*(9), 1023–1050. https://doi.org/10.1002/nag.657

Omidvar, M., Chen, Z., & Iskander, M. (2014). Image-Based Lagrangian Analysis of Granular Kinematics. *Journal of Computing in Civil Engineering*, *29*(Dic), 4014101. https://doi.org/10.1061/(asce)cp.1943-5487.0000433

Riyahi-Alam, S., Peroni, M., Baroni, G., & Riboldi, M. (2014). Regularization in deformable registration of biomedical images based on divergence and curl operators. *Methods of Information in Medicine*, *53*(1), 21–28. https://doi.org/10.3414/ME12-01-0109

Rechenmacher, A. L., & Saab, N. A. (2002). Digital image correlation (DIC) to evaluate progression and uniformity of shear bands in dilative sands. *15th ASCE Engineering Mechanics Conference (Em 2002)*, (Dic), 1–8.

Rechenmacher, A. L., & Finno, R. J. (2004). Digital Image Correlation to Evaluate Shear Banding in Dilative Sands. *Geotechnical Testing Journal*, *27*(1), 13–22. https://doi.org/10.1520/GTJ11263J

Rechenmacher, A. L. (2005). *Onset, growth, progression and uniformity of shear bands in dilative sands*. *ICF XI - 11th International Conference on Fracture*. Retrieved from http://www.icf11.com/proceeding/EXTENDED/5076.pdf

Rechenmacher, A. L. (2006). Grain-scale processes governing shear band initiation and evolution in sands. *Journal of the Mechanics and Physics of Solids*, *54*(1), 22–45. https://doi.org/10.1016/j.jmps.2005.08.009

Rechenmacher, A. L., Abedi, S., Chupin, O., & Orlando, A. D. (2011). Characterization of mesoscale instabilities in localized granular shear using digital image correlation. *Acta Geotechnica*, *6*(4), 205–217. https://doi.org/10.1007/s11440-011-0147-2

Riyahi-Alam, S., Peroni, M., Baroni, G., & Riboldi, M. (2014). Regularization in deformable registration of biomedical images based on divergence and curl operators. *Methods of Information in Medicine*, *53*(1), 21–28. https://doi.org/10.3414/ME12-01-0109

Roscoe, K.H., Arthur, J.R.F. and James, R.G. (1963). "The determination of strains in soils by an X-ray method", Civ. Eng. Public Works Rev., 58, 873–876 and 1009–1012.

Roters, F., Eisenlohr, P., Hantcherli, L., Tjahjanto, D. D., Bieler, T. R., & Raabe, D. (2010). Overview of constitutive laws, kinematics, homogenization and multiscale methods in crystal plasticity finite-element modeling: Theory, experiments, applications. *Acta Materialia*, *58*(4), 1152–1211. https://doi.org/10.1016/j.actamat.2009.10.058

Song, A. (2012). Deformation analysis of sand specimens using 3D digital image correlation for the calibration of an elasto-plastic model. Ph.D. Dissertation, Texas A&M University, College Station, TX.

Sjödahl, M., Siviour, C. R., & Forsberg, F. (2012). Digital volume correlation applied to compaction of granular materials. In *Procedia IUTAM* (Vol. 4, pp. 179–195). https://doi.org/10.1016/j.piutam.2012.05.020

Sutton, M. A., Orteu, J. J., & Schreier, H. W. (2009). Image Correlation for Shape, Motion and Deformation Measurements- Basic Concepts, Theory and Applications. *Image Rochester NY*, 341. https://doi.org/10.1007/978-0-387-78747-3

Takano, D., Lenoir, N., Otani, J., & Hall, S. A. (2015). Localised deformation in a wide-grained sand under triaxial compression revealed by X-ray tomography and digital image correlation. *Soils and Foundations*, *55*(4), 906–915. https://doi.org/10.1016/j.sandf.2015.06.020

Tiwari, V., Sutton, M. A., McNeill, S. R., Xu, S., Deng, X., Fourney, W. L., & Bretall, D. (2009). Application of 3D image correlation for full-field transient plate deformation measurements during blast loading. *International Journal of Impact Engineering*, *36*(6), 862–874. https://doi.org/10.1016/j.ijimpeng.2008.09.010

Tschudi, M. A., Maslanik, J. A., & Perovich, D. K. (2008). Derivation of melt pond coverage on Arctic sea ice using MODIS observations. *Remote Sensing of Environment*, *112*(5), 2605–2614. https://doi.org/10.1016/j.rse.2007.12.009

Viggiani, G., & Hall, S. (2008). Full-field measurements, a new tool for laboratory experimental geomechanics. *... of the 4th International Symposium on ...*, (1984), 3–26. Retrieved from http://books.google.com/books?hl=en&lr=&id=0DAZEjBclqkC&oi=fnd&pg=PA3&dq=Full-+field+measurements,+a+new+tool+for+laboratory+experimental+ geomechanicz&ots=DpEEjm1M1m&sig=bmoITE_jUoujr1SHzXvSj43-KJo

Wattrisse, B., Chrysochoos, A., Muracciole, J. M., & Némoz-Gaillard, M. (2001). Kinematic manifestations of localisation phenomena in steels by digital image correlation. *European Journal of Mechanics, A/Solids*, *20*(2), 189–211. https://doi.org/10.1016/S0997-7538(00)01113-X

Wriggers, P. (2008). *Nonlinear Finite Element Methods*. *Book*. https://doi.org/10.1007/978-3-540-71001-1

Zhang Z., & Chen Q. (2007). Comparison of the Eulerian and Lagrangian methods for predicting particle transport in enclosed spaces. *Athmospheric Environment, 41* (25), 5236-5248. linkinghub.elsevier.com/retrieve/pii/S1352231007002786